

Adsorption Behavior of Congo Red on Carbon Materials Based of Humic Acid

An Wang

North China University of Science and Technology

Boyuan Li

North China University of Science and Technology

Yatong Wang

North China University of Science and Technology

Xiaoran Sun (✉ xiaoranhb@sohu.com)

North China University of Science and Technology

Simeng Bian

North China University of Science and Technology

Hongzhou Shang

North China University of Science and Technology

Zheng Zhao

North China University of Science and Technology

Kaili Fan

North China University of Science and Technology

Research Article

Keywords: Humic acid, Congo red, Adsorption, Kinetic, Isotherm

Posted Date: May 17th, 2021

DOI: <https://doi.org/10.21203/rs.3.rs-516247/v1>

License:  This work is licensed under a Creative Commons Attribution 4.0 International License.

[Read Full License](#)

Version of Record: A version of this preprint was published at New Journal of Chemistry on January 1st, 2021. See the published version at <https://doi.org/10.1039/D1NJ03926A>.

Adsorption behavior of Congo red on carbon materials based of humic acid

An Wang^a, Boyuan Li^a, Yatong wang^a, Xiaoran Sun^{a,*}, Simeng Bian^a, Hongzhou Shang^b, Zheng Zhao^a, Kaili Fan^a

^a School of Chemical Engineering, North China University of Science and Technology, Tangshan 063210, China

^b School of material science and Engineering, North China University of Science and Technology, Tangshan 063210, China

* Corresponding author at: School of Chemical Engineering, North China University of Science and Technology, Tangshan 063210, China

E-mail addresses: xiaoranhb@souhu.com

Abstract: In this study, a carbon composite based on humic acid (CAH) was synthesized by partially carbonizing humic acid by using aluminum sulfate with a mass ratio of 2:3 and a leavening agent oxalic acid with a fixed mass. The morphology and microstructure of the sample are measured by scanning electron microscope (SEM), x-ray diffractometer (XRD), thermal analysis (TG-DSC), Raman spectroscopy (Raman), X-ray photoelectron spectroscopy (XPS) and Fourier Transform infrared spectroscopy (FT-IR) is used to analyze the composition and structure of materials. The BET surface area of CAH is determined to be 149 m²/g. Congo red was used as a model adsorbent for adsorption research. When the dye concentration is 400 mg/L and 10mg of adsorbent powder is used. CAH has the highest dye removal rate of adsorption capacity. The pseudo-first-order and pseudo-second-order kinetic models were used to describe the kinetic data and the Langmuir and Freundlich models were applied to describe the adsorption isotherms. The results showed that the equilibrium adsorption data were found to fit better to the Langmuir adsorption model and the kinetic process of adsorption could be described by the pseudo-second-order model. Compared with humic acid, CAH composite materials can effectively improve the adsorption rate and adsorption capacity of Congo red, and the adsorption capacity is as high as 3986mg/g within 30 minutes. In addition, considering the cost issue, this study selected low-cost humic acid as a carbon source to prepare composite materials, emphasizing the importance of cost.

Key words: Humic acid, Congo red, Adsorption, Kinetic, Isotherm

1. Introduction

Water is the source of human life, and the existence of water is vital to human survival. However, in recent years, water resources have gradually been in short supply, and at the same time the discharge of polluted wastewater has increased^{[1],[2]}. Effective treatment of polluted wastewater is imperative. In the past few decades, the global water quality has deteriorated seriously, mainly due to rapid population growth, unplanned urbanization, rapid industrialization and excessive use of natural water resources. The main sources of water pollution include the discharge of untreated sanitary and toxic industrial waste, and dumped industrial wastewater. In recent years, various toxic chemicals/compounds^[3]. Such as micro-pollutants, personal care products, endocrine disrupting compounds, pesticides, inorganic anions. Have been detected in drinking water in many places^[4]. Therefore, it is still a huge scientific and engineering challenge to develop an environmentally friendly and inexpensive method to treat pollutants in wastewater^[5].

Dyes are a class of organic compounds that can dye other substances. With the continuous economic development, they are widely used in many industrial fields such as textiles, papermaking, food, pharmaceuticals, leather, plastic, rubber, and cosmetics^{[6],[7],[8]}. At present, a large amount of dye wastewater is discharged into the environment, causing serious environmental pollution problems^[9]. According to reports, my country produces more than 700,000 tons of different dyes each year, and 5% to 10% of these dyes are lost during the dyeing process, and more than 20% of the increasingly serious sewage pollution comes from the above dyes^{[10],[11]}. Most dyes are water pollutants that seriously harm the environment and organisms^[12]. The untreated discharge of these dye wastewaters will not only destroy the aquatic ecosystem, affect the aquatic biota, but also cause irreversible and remediation damage to the soil^{[13],[14]}. It has teratogenic, carcinogenic, and mutagenic properties in the human body, and its high-water solubility can easily move with the water body after being discharged, causing harm to more organisms and even human health^{[15],[16],[17]}.

Congo red is a typical anionic azo dye. Its physical and chemical properties is listed in Table 1 below^{[18],[19],[20],[21]}. Due to its complex aromatic structure, high chemical stability and thermal stability. Congo red is an organic pollutant

that can increase the chemical oxygen demand of water and is extremely difficult to degrade^{[22],[23]}. Under anaerobic conditions, the degradation product of Congo Red is benzidine, which is an internationally recognized carcinogen^{[24],[25]}. Therefore, there is an urgent need to develop an environmentally friendly and efficient material to remove excess Congo red in water to solve the current environmental problem^{[26],[27]}.

Table 1. Physicochemical characteristics of CR

CAS No.	573-58-0
CA Index name	Disodium 4-amino-3-[4-[4-[(1-amino-4-sulfonato-2-naphthyl) azo] phenyl] phenyl] azo-naphthalene-1-sulfonate
Molecular formula	C ₃₂ H ₂₂ N ₆ Na ₂ O ₆ S ₂
Molecular weight	696.66300
Appearance and Character	Brown-red powder
Density	0.995g/mL at 25°C
Melting point	360°C
pKa	4.1
Color change at pH	Blue (3.0) to red (5.0)
UV-vis (λ_{\max})	496 nm, 488 nm, 595 nm
Water solubility	Soluble
Stability	Stable. Incompatible with strong oxidizing agents.

After processing, the carbon composite material has a high specific surface area, a highly developed pore structure and surface activity^{[28],[29],[30]}. These properties make it have extremely high adsorption performance. It is one of the most powerful adsorption materials for adsorbing dye molecules, heavy metals, and organic pollutants^{[31][32][33]}. Carbon composite materials are used in the treatment of sewage and wastewater with their excellent adsorption performance and catalytic degradation performance^{[34],[35],[36],[37]}.

This article introduces a simple method for preparing CAH using economical and environmentally friendly humic acid as a carbon source and catalytically calcining at high temperatures. Using SEM, TEM, FT-IR, BET, TG-DSC, XRD, XPS, Raman and other analytical methods to characterize CAH, and for the first time as a high-efficiency adsorbent for removing Congo red in aqueous solution. Discussion on the influencing factors of adsorption capacity and exploration of the adsorption mechanism.

2. Material and methods

2.1. Material

Humic acid was purchased from West Asia Chemical Technology Co., Ltd., with a molecular weight of 227 and a purity of 98%. Anhydrous aluminum sulfate and oxalic acid were purchased from Macklin Reagent Co., Ltd., and Congo Red was purchased from Aladdin Reagent Co., Ltd., both analytical reagents.

2.2. Preparation of CAH

Dissolve 5g of HA in 100 mL of 15% HNO₃ solution, dissolve it ultrasonically for 20 minutes, let it stand for a period of time and then filter with suction to dry the sample. Then take the above-mentioned nitrated HA and dissolve it in 100mL 25% concentrated H₂SO₄, heat it in a water bath at 80°C, condense and reflux for 3.5h, stand still for 40min, wait for the solid to settle, filter and dry the solid product. Then dissolve the above-mentioned dry product in 120 mL of 25% NaOH solution, stir for 2 hours at room temperature, and centrifuge (3000r/min, 8min) for the solid product. Then

add 20 mL of concentrated HCl, and after solid precipitation, filter and dry to obtain sulfonated humic acid.

Take 1g of sulfonated HA, 1.5g of $Al_2(SO_4)_3$, and 1g of $C_2H_2O_4$ in a mortar to fully grind and mix. Then, it was heated to $400^\circ C$ for 3 hours at $15^\circ C/min$ in a vacuum tube furnace under nitrogen atmosphere to obtain gray powder, namely humic acid-based aluminum-carbon composite material (CAH).

2.3 Characterization methods

Using the Hatachi S4800 field emission scanning electron microscope from Hitachi, Japan, when the test scanning acceleration voltage is 10kV, photographs and observations under different magnifications are taken. The TEM of the sample to be tested was performed on Jeol Jem-2100F, in a vacuum environment, for observation operations related to the transmission electron microscope. Under your condition that the laser wavelength is 532nm and the test record range is $10\sim 3500cm^{-1}$. Use the DXR laser Raman spectrometer of American Thermoelectric Company. The fully dried sample is spectrally scanned with Thermo ESCALAB 250xi, and the percentage of carbon and oxygen in the functional groups in the sample is calculated. After the sample is dried, it is heated to $800^\circ C$ at a rate of $2^\circ C/min$ under the condition of an initial temperature of $30^\circ C$ under a high-purity nitrogen atmosphere. Test after weighing the sample. After drying the sample in an oven at $100^\circ C$ for 24 hours, the solid powder to be tested is vacuum degassed overnight at a temperature of $100^\circ C$, using liquid nitrogen as the adsorption medium, and measuring with high purity at liquid nitrogen temperature (77 K) Relative pressure.

2.4 Adsorption experiments

Measure 100mL of the CR aqueous solution with a concentration of 400mg/L in a 250mL small beaker, add 10mg CAH to the CR aqueous solution, take 5ml of the solution at certain intervals under magnetic stirring, and centrifuge the supernatant with ultraviolet-visible spectroscopy The photometer measures the absorbance value A of the solution at 498nm, and obtains the concentration of CR in the solution according to the standard curve, thereby calculating the saturated adsorption amount q_e . The calculation formulas are shown in (1), (2):

$$q_t = \frac{(c_0 - c_t)V}{m} \quad (1)$$

$$q_e = \frac{(c_0 - c_e)V}{m} \quad (2)$$

Where C_0 and C_e are the initial and equilibrium concentrations of CR (mg/L); m is the weight of the adsorbent used and V is the volume of the aqueous solution. The datum was then fitted in adsorption isotherm, kinetic models and thermodynamic models.

Weigh 10 mg of the dried CAH and soak it in 100 mL of 100 mg/L CR aqueous solution and distilled water at $25^\circ C$. Take out the CAH every 5 min and weigh it. The total swelling time is 60 min. After removing the CAH each time, wipe off the moisture on the surface with filter paper, and then weigh it. The calculation formula of swelling rate is as follows (3):

$$SR = \frac{W_t - W_0}{W_0} \quad (3)$$

In the formula, SR is the swelling rate (%), W_0 is the mass before swelling (mg), and W_t is the mass after CAH swelling at time t (mg).

3. Results and discussion

3.1 Characterization Techniques

3.1.1 Scanning electron microscope (SEM) and transmission electron microscope (TEM)

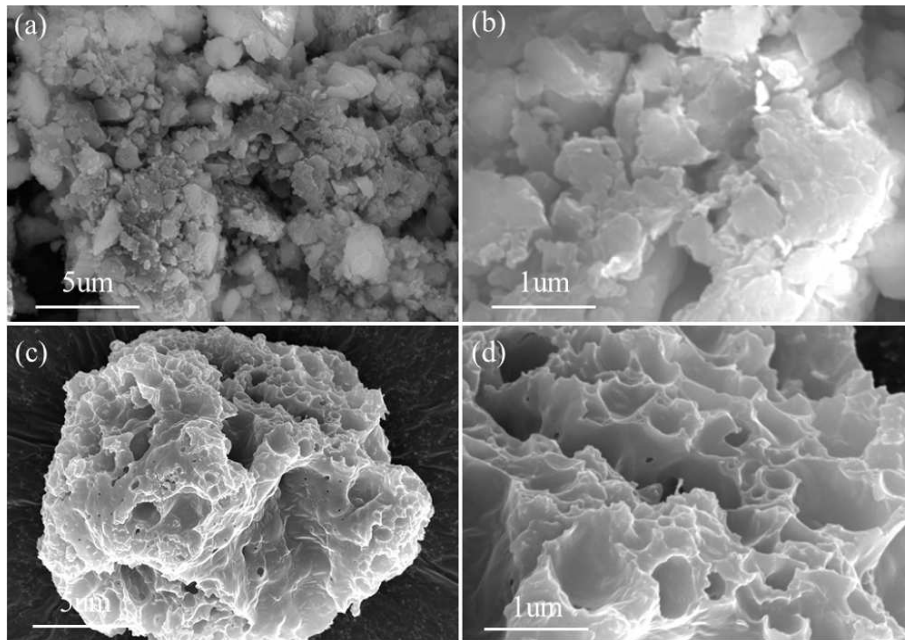


Fig. 1 SEM of the HA (a, b) and CAH (c, d)

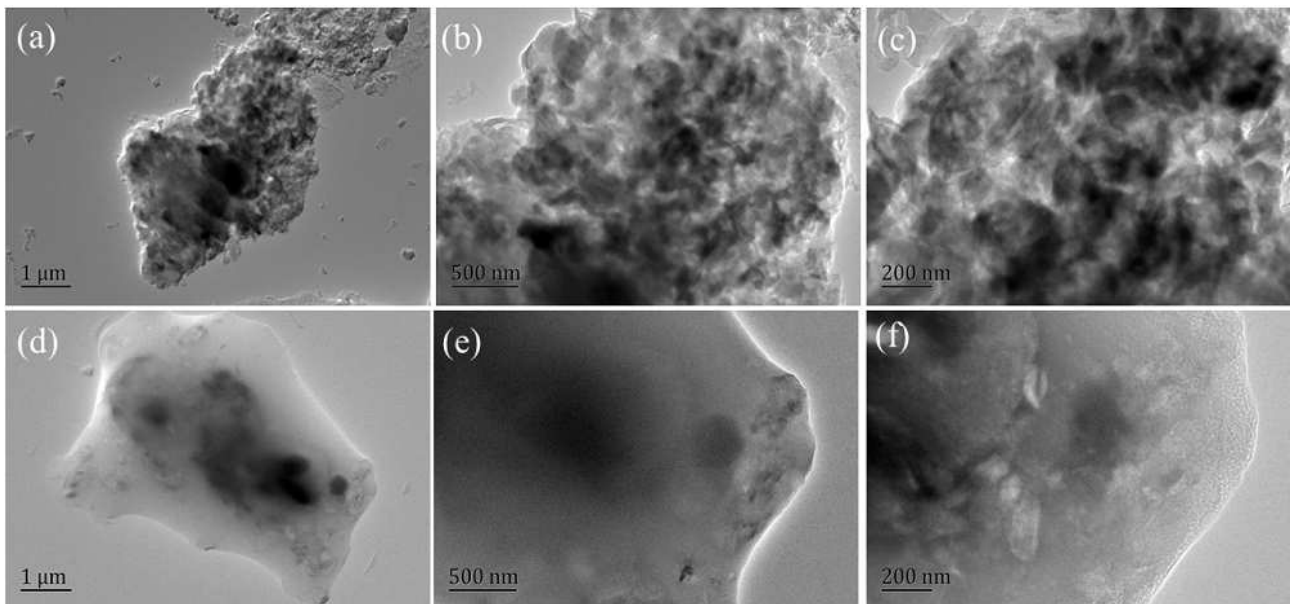


Fig. 2 TEM of the HA (a, b, c) and CAH (d, e, f)

Figure 1 (a, b) and Figure 2 (a, b, c) are the SEM and TEM images of HA. Both the SEM and TEM images show that the surface of HA exhibits a densely packed structure. This may be due to the fact that the surface of HA particles contains too many -COOH and -OH functional groups and a large number of aromatic structure-related interactions. Figure 1 (c, d) is the SEM image of CAH. It can be seen from the figure that compared with HA, the surface of CAH prepared by the reaction of HA and aluminum sulfate has a large number of cauliflower-like porous structures, and the edge thickness has changed significantly Thin, the specific surface area increases, and the developed specific surface area

helps the material and the dye molecule contact and adsorb, and promotes the adsorption reaction. Figure 2 (c, d, e) shows the TEM images of HA and CAH. The TEM image of HA shows that its surface is smooth and thick. Compared with HA, the TEM image of CAH has obvious lattice fringes, thinner layer and obvious hole-like structure at the edge.

3.1.2 Fourier transforms infrared spectroscopy (FT-IR)

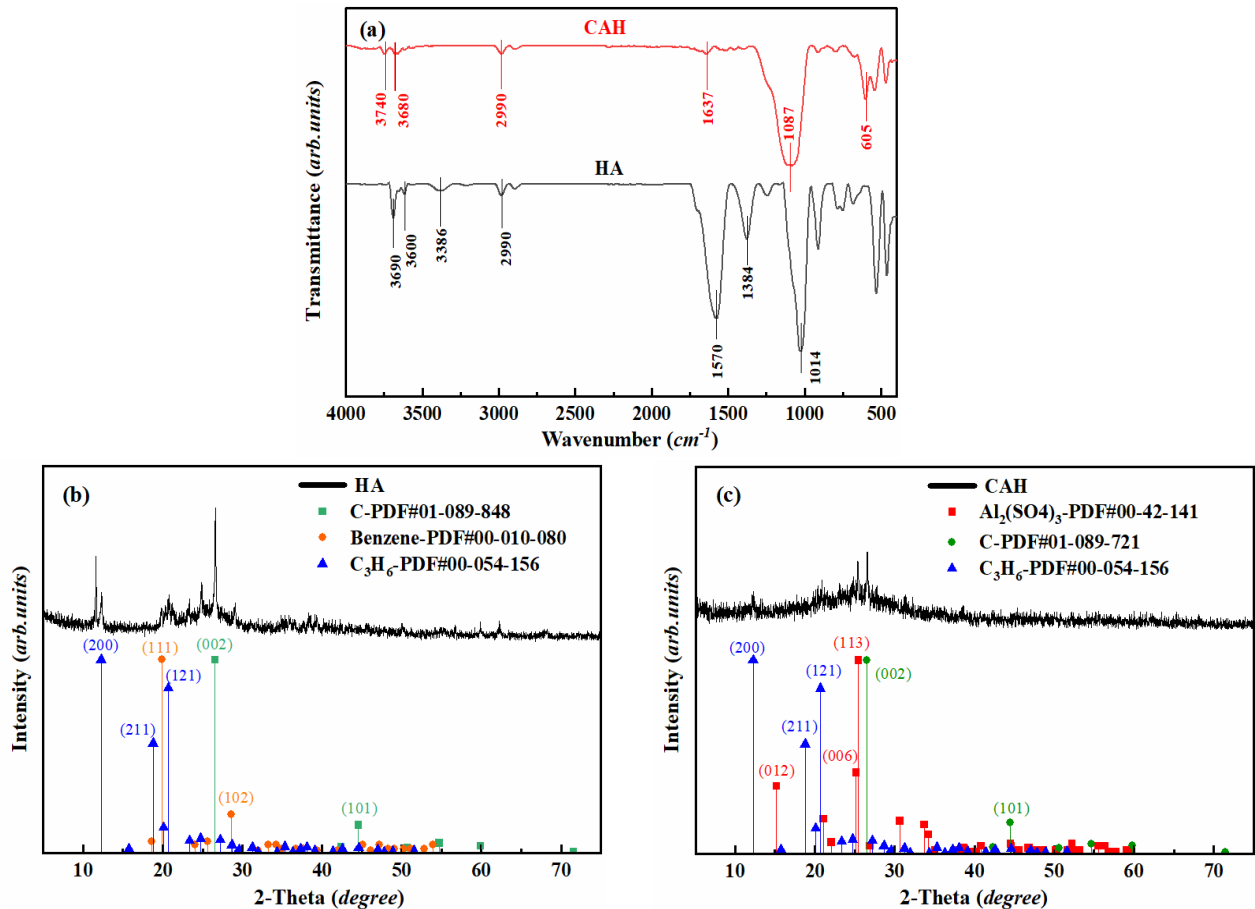


Fig. 3 FT-IR of the HA and CAH (a); XRD patterns of HA and HA base peak (b), patterns of CAH and CAH base peak (c)

Figure 3(a) shows the infrared spectra of HA and CAH. CAH has a broad blunt peak at $3750cm^{-1}$, which is the characteristic peak of the stretching vibration of the Association -OH. $1570-1637cm^{-1}$ may be the aromatic C=C stretching vibration, and the peak produced by CAH is obviously weaker than that produced by HA. This may be the reason for the fracture and reorganization of a large number of aromatic ring structures after high temperature burning^{[38][39][40]}. The bending vibration peak of -CH and the bending vibration peak of O-H are at $1384cm^{-1}$. CAH is very weak at about $1300cm^{-1}$, which means that the branch chain breaks after high temperature burning, and carbon dioxide and water vapor are released. In addition, the peak of CAH at about $1087 cm^{-1}$ is the characteristic peak of flexural vibration of Al-O-Al; and at $605 cm^{-1}$ is the characteristic peak of flexural vibration of Al-OH surface, which indicates that HA and $Al_2(SO_4)_3$ are in the reaction process. Polyaluminum is formed, which is connected by a hydroxyl bridge and an oxygen bridge to form a polymer with a network cross-linked structure.

3.1.3 X-ray diffraction spectrum (XRD)

Figure 3 (b, c) are the XRD patterns of HA and CAH and the standard cards of the substances contained in them. The results show that HA and CAH have peaks at $2\theta=26.6^\circ$, indicating the presence of crystal structure carbon. As the temperature increases, the XRD pattern in $2\theta=26.6^\circ$ represents the diffraction peak of the carbon (002) crystal plane gradually becoming sharper, indicating that the degree of graphitization increases with the calcination temperature. It can be seen from the figure that HA has an obvious aromatic structure, while the aromatic structure of CAH is not obvious,

which also proves that the carbonized benzene ring after high temperature has broken and reorganized. In Figure 3(c), the (012), (006), and (113) crystal planes are the peaks representing aluminum, which proves that aluminum and humic acid are compounded together^[41].

3.1.4 Raman spectrum analysis

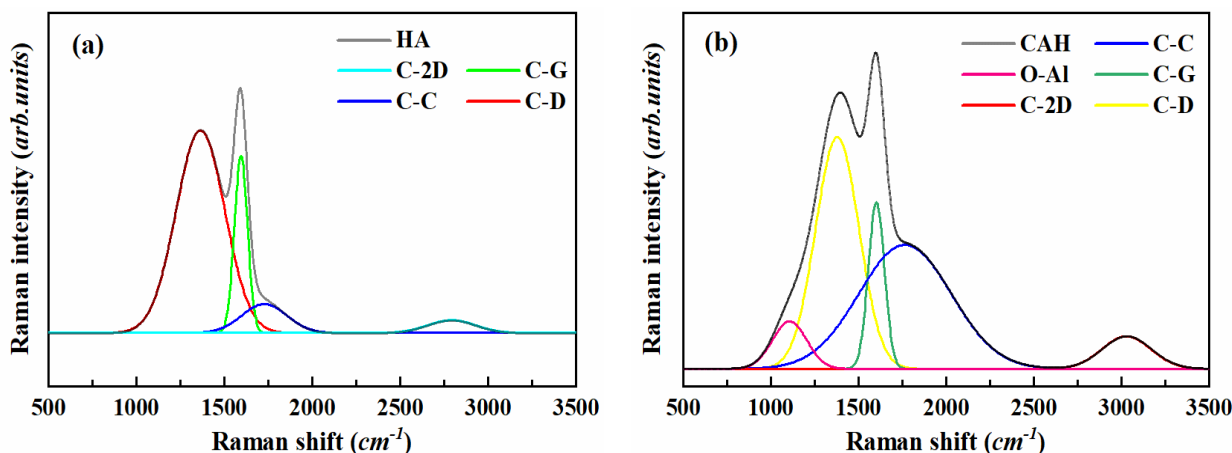


Fig 4. Raman spectrum of the HA (a) and CAH (b)

Figure 4 (a, b) shows the Raman spectra of HA and CAH. Both HA and CAH Raman spectra show D-peak (1350 cm^{-1}), G-peak (1580 cm^{-1}) and 2D-peak (2700 cm^{-1}). The ratio of D-peak intensity (ID) and G peak intensity (IG) (ID/IG) indicates the degree of sp^2 hybridization defects of the material. The higher the ratio, the more defects, that is, more non- sp^2 hybrid structures. Now the ID/IG value of HA is 1.15, and the ID/IG value of CAH is 1.38, which indicates that the non- sp^2 hybrid structure in CAH is reduced compared with that in HA. This may be because the presence of oxygen in the air causes the carbon-carbon double bond to be oxidized, and the saturated structure increases, and the layered polymer aluminum network cross-linked structure verified in the infrared spectrum of Figure 3 (a) is connected by a hydroxyl bridge and an oxygen bridge saturated structure. Correspondingly, it is also consistent with the increase of C-O structure in the XPS characterization results.

3.1.5 X-ray photoelectron spectroscopy analysis (XPS)

Figure 5 shows that both materials contain C and O elements. Figures 5(b, d) are the C1s peaks of humic acid and aluminum-carbon materials, respectively. Corresponding to the part of the binding energy of $280\text{ eV}\sim 294\text{ eV}$ in HA and CAH in Figure 5(a, b). The peak split diagram of C1s shows that HA and CAH have four different peaks at the center of binding energy of 284.35 eV , 285.6 eV , and 288.3 eV , which are C-C, C-O, and C=O. And their content in HA and CAH is different. The content of HA in C-C is 75.30%, C-O is 14.69%, and C=O is 10.01%. The content of C-C in CAH is 55.66%, C-O is 24.83%, C=O is 19.51%, the saturated structure of C-O increases, and the saturated structure of C-C decreases, indicating that the saturated structure has changed, which is conducive to the formation of a network cross-linked structure by the hydroxyl bridge and oxygen bridge connecting aluminum. Figure 5(c) shows that CAH contains Al element, which corresponds to the part of the binding energy of $84\text{ eV}\sim 66\text{ eV}$ in Figure 5(c). There is a characteristic peak at 75.15 eV , which corresponds to the satellite peak of Al2p, which is the characteristic peak of Al^{3+} .

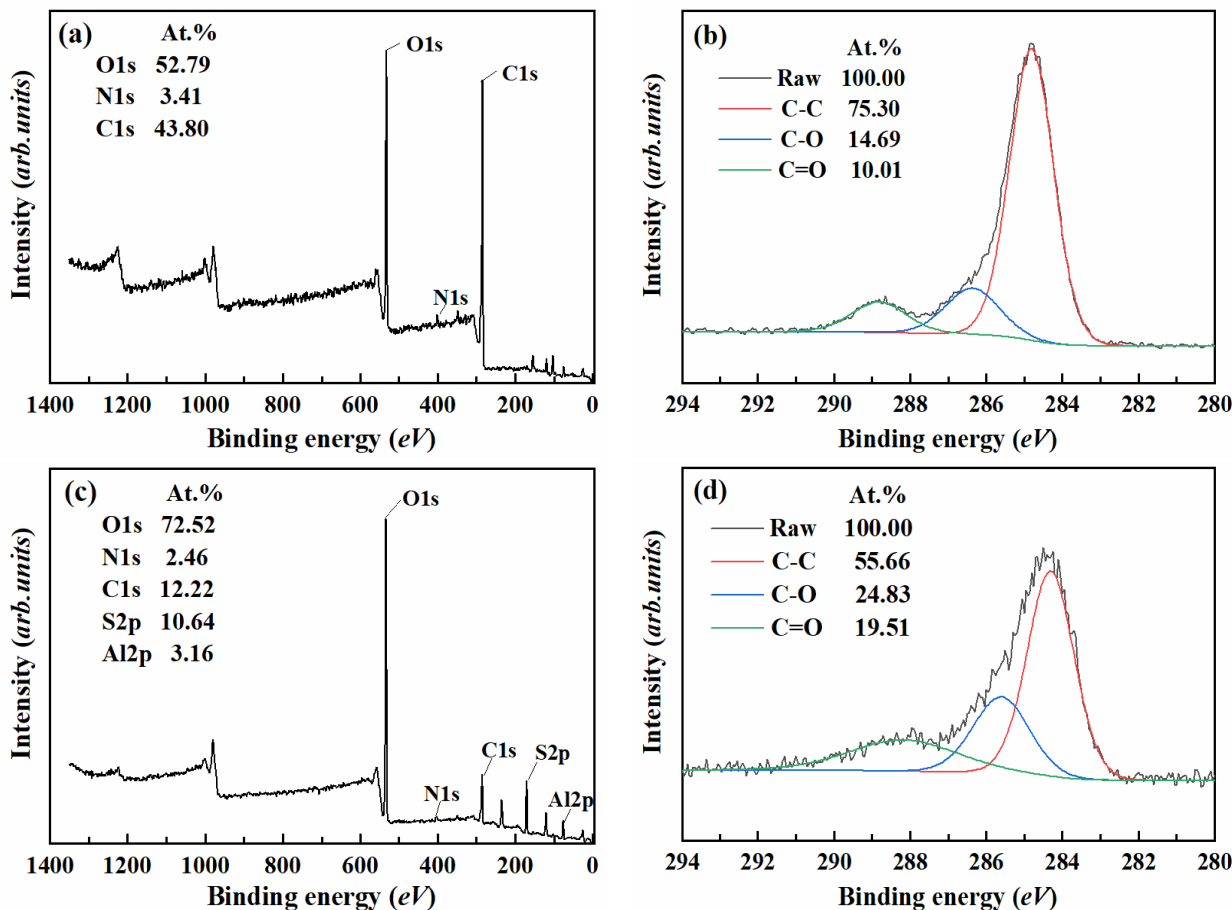


Fig. 5 XPS total peaks of HA and CAH (a, c); C1s peaks of HA and CAH (b, d)

3.1.6 Thermogravimetric Analysis (TG-DSC)

Figure 6 (a, c) shows the TG-DTG curves of HA and CAH. It can be seen from Fig. 6 that the CAH pyrolysis process has gone through three stages, namely 20°C~105°C, 105°C~575°C and 575°C~800°C. Weight loss at 20°C~105°C is the removal of adsorbed water and adsorbed gas in CAH. Adsorbed water and adsorbed gas are connected to CAH through weak intermolecular force between CAH, which is easy to desorb. A very slow weight loss occurs at 105°C~400°C, which may be due to the decarboxylation of carboxyl groups and the cleavage of some oxygen-containing bonds, resulting in water and carbon dioxide, and the quality is slightly reduced. This indicates that CAH has good thermal stability at 400°C. The weight loss rate of HA is very high at 145°C~250°C, which mean that in the range of 105°C~400°C, CAH has better thermal stability than HA. After 400°C to 575°C, both CAH and HA lose more weight. It can be seen from the DSC curve in Fig. 6 (b, d) that the pyrolysis rate in this stage also gradually increases, especially after 400°C, the pyrolysis rate increases sharply. There are many reasons for weight loss, including the cleavage of bridge bonds to generate free radicals, the cleavage of oxygen-containing heterocyclic compounds and irregular aromatics, and the cleavage of most oxygen-containing functional groups to generate small molecular gas such as carbon dioxide and water. Between 575°C and 800°C, the weight loss rate of CAH is higher than that of HA, which may be related to the catalytic acceleration of the decomposition process caused by aluminum ions in CAH. The overall results show that after 400°C, CAH gradually decomposes with the increase of temperature, and the thermal stability becomes worse. With the decomposition of the activated structure and active functional groups that play a role in the adsorption process, the removal rate of CAH to CR gradually decreases. The temperature of the CAH preparation process has a corresponding effect on the CR removal rate. After 400°C, the CR removal rate is significantly reduced in CAH, which is caused by the decomposition of the CAH structure^[42].

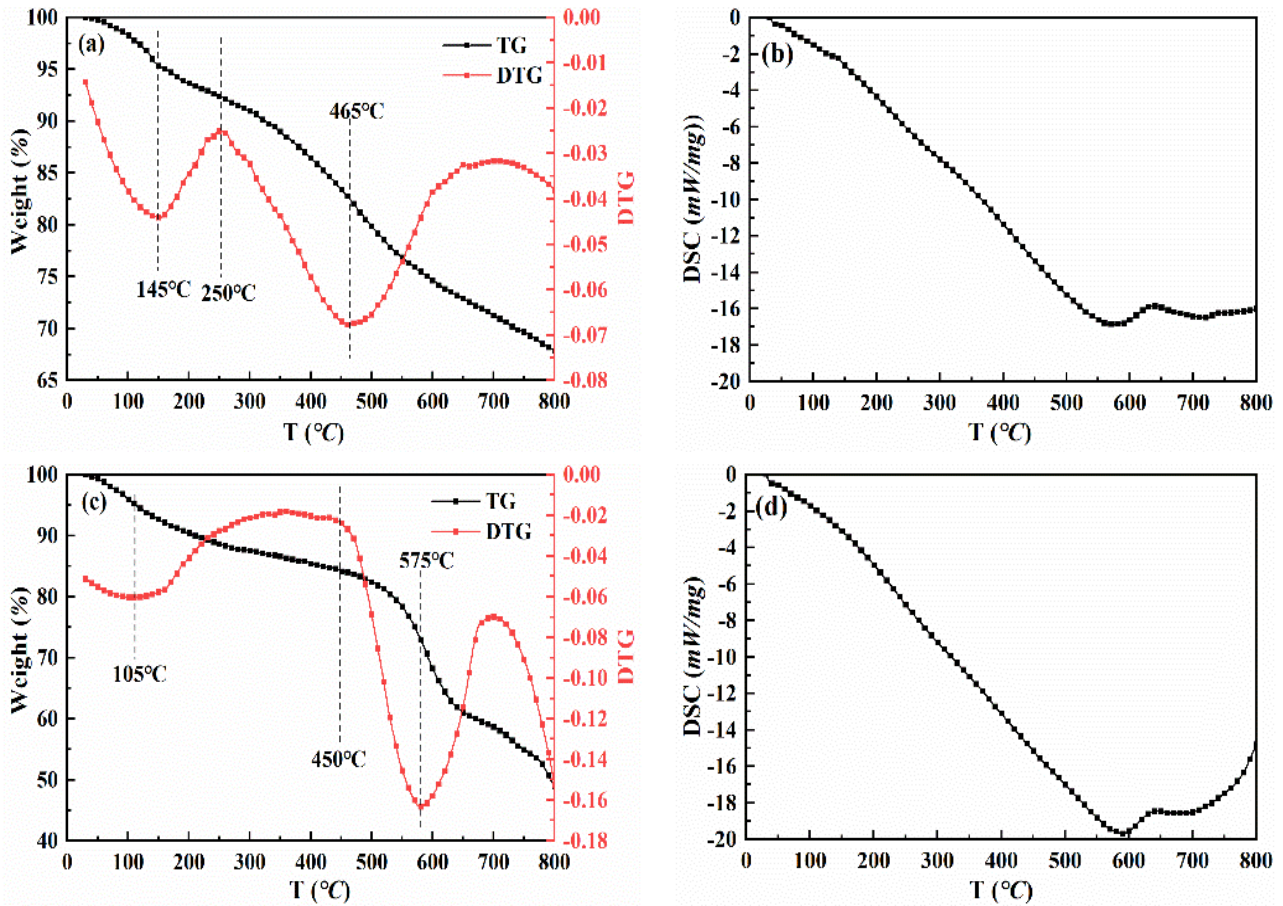


Fig.6 TG-DSC of the HA (a, b) and CAH (c, d)

3.1.7 Specific surface area test analysis (BET)

The N_2 adsorption isotherm of HA was studied by N_2 adsorption-desorption isotherm, as shown in Figure 7. After calculation, its specific surface area is $6.19\text{m}^2/\text{g}$, pore volume is $0.040\text{cm}^3/\text{g}$, and the pore size distribution is uniform, with an average of about 26.19nm , and this indicates that there may be fewer pores in the HA particles. The reason for the existence of pores may be gaps formed when many HA particles are brought together due to agglomeration. The porosity and specific surface area of the prepared CAH were studied by N_2 adsorption-desorption isotherm. As showed in Figure 7(a, b), the adsorption and desorption speed of CAH and HA is not completely consistent, that is, the desorption curves do not completely overlap, but H3 typical hysteresis loops appear. The reason is that the layered structure of the material is formed during the accumulation slits, cracks and wedge-shaped structures. This is consistent with the layered image of SEM. After calculation, specific surface area of CAH is $149.90\text{m}^2/\text{g}$, the pore volume is $0.41\text{cm}^3/\text{g}$, and the pore size distribution is about 12.16nm , so CAH is a malodorous material. Compared with HA, the specific surface area of CAH is significantly increased, which is also consistent with the results of the SEM scan^{[43],[44]}.

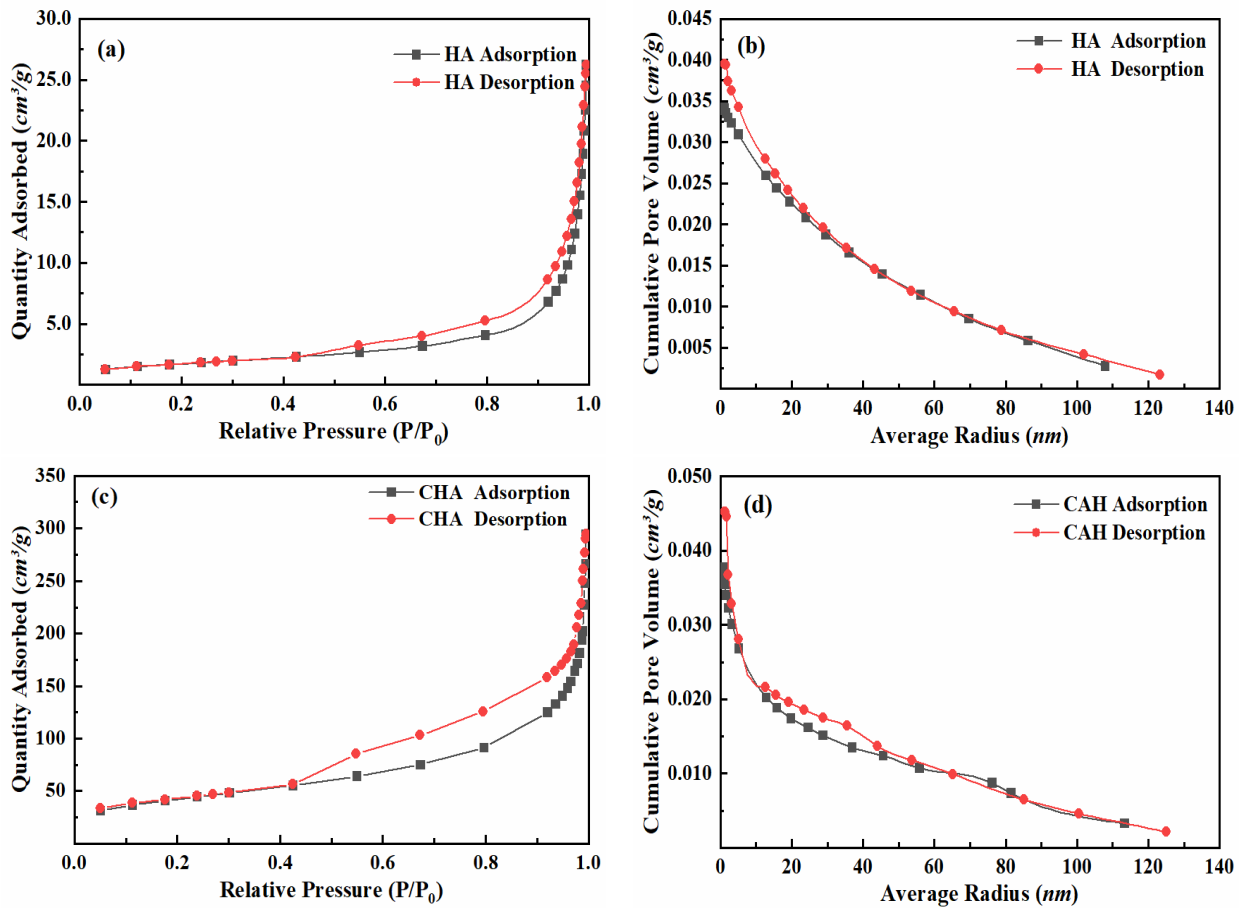


Fig.7 BET of the HA (a, b) and CAH (c, d)

3.2 Adsorption studies

3.2.1 Effect of adsorbent dosage

Figure 8(a) shows the effect of different quantities of CAH on the adsorption performance of CR. It can be seen from the figure that with the increasing amount of CAH, the adsorption capacity of CR first increased from 2.71g/g to 3.98g/g and then decreased to 2.68g/g. In summary, the reason may be that as the amount of adsorbent CAH increases, the number of active sites that can adsorb CR molecules in CAH also increases. But when the CAH reaches a certain number, that is to say, when the active adsorption site provided by CAH is equal to the amount of CR molecules, the adsorption of CAH to CR reaches saturation and adsorption equilibrium occurs. Although the amount of adsorbent continues to increase, the total amount of adsorption on CR no longer increases, so the amount of adsorption begins to decrease.

3.2.2 Effect of initial concentration

Figure 8(b) shows the effect of different concentrations of CR on the adsorption capacity. It can be seen from the figure that as the concentration of CR increases, the amount of CAH adsorbed on CR first increases and then decreases. At 100mg/L, the adsorption capacity is 1.00g/g, then with the gradual increase of the initial concentration, the adsorption capacity of CAH to CR shows an increasing trend. When the concentration increases to 400mg/L, the adsorption capacity reaches the maximum 3.96g/g. With the increase of CR concentration, the adsorption capacity also began to decrease. This is because when the amount of adsorbent is determined, the active adsorption sites on the adsorbent are also constant. Therefore, when the adsorption of CAH to CR reaches equilibrium, no matter how the amount of adsorbent CAH increases, the total amount of adsorption will not change, resulting in a decrease in adsorption capacity.

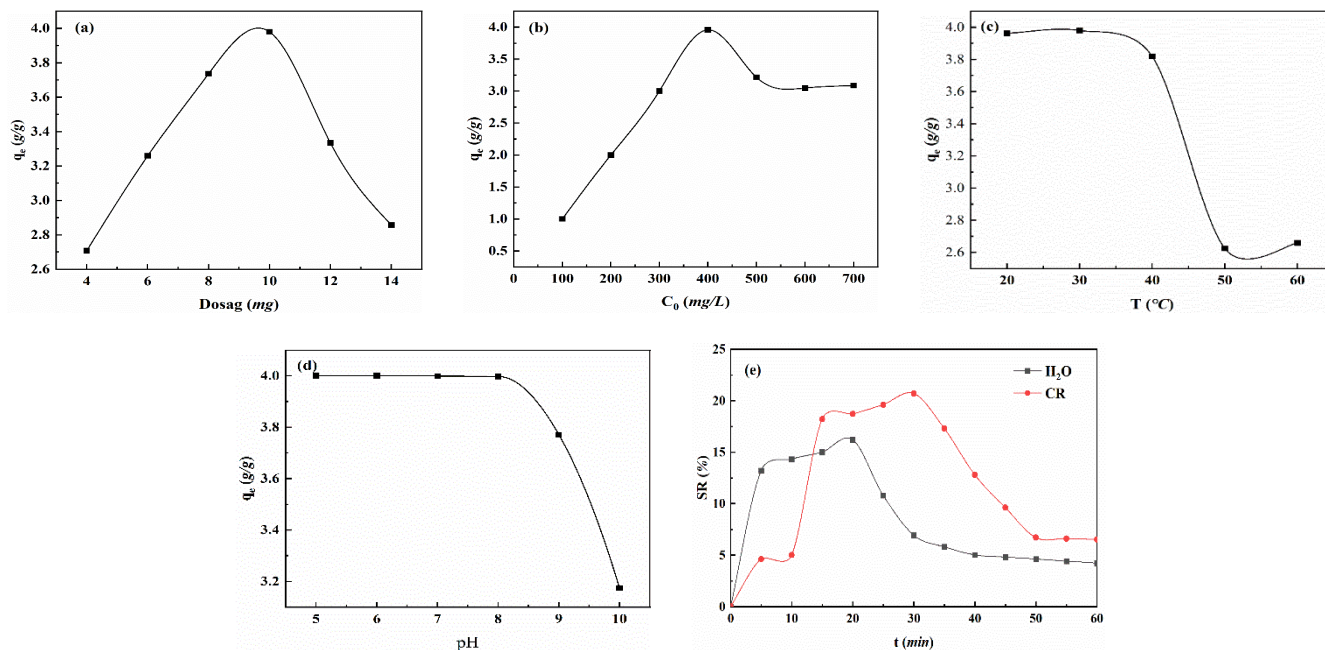


Fig.8 The effect of the initial concentration of CR on the adsorption capacity (a) and removal rate (b); the effect of temperature (c) and pH (d) on the adsorption capacity impact; the effect of time on SR of CAH (e).

3.2.3 Effect of solution temperature

Figure 8(c) shows the effect of CHA on the adsorption capacity of CR under different adsorption temperature conditions. It can be seen from the figure that in the temperature range of 25-40°C, as the temperature increases, the adsorption capacity of CHA on CR decreases slightly, but it can remain basically unchanged. It shows that in this temperature range, temperature has little effect on the adsorption capacity. But when the temperature is higher than 40°C, the adsorption capacity of CAH to CR begins to decrease sharply. The possible reason is that on the one hand, too high temperature will destroy the structure of the CAH surface, and the bond formed by the combination between CR and the oxygen-containing functional group on the CAH surface will be destroyed, making the adsorption hindered. The adsorption capacity drops. On the other hand, the adsorption behavior is a dynamic equilibrium. The increase in temperature within a certain range can promote the thermal movement of CR molecules and promote their contact with the CAH surface to be adsorbed, but it may also cause the adsorption of the CR molecules on the CAH surface. CR molecule separates from a large amount of CAH more quickly. At this time, the desorption rate is higher than the adsorption rate, which instead promotes desorption and makes the adsorption behavior difficult.

3.2.4 Effect of solution pH

The structure of CR changes under strong acidic conditions with a pH lower than 5, so the pH range for this experiment is 5-10. Under different pH conditions, the influence of CAH on the adsorption performance of CR was investigated, and the results are shown in Figure 8(d). In the pH range of 5~8, the difference in the adsorption capacity of CAH to CR is not very large, and shows a relatively stable trend. At pH=6, the maximum adsorption capacity is 4.00g/g. But when the pH increased to 10, the adsorption capacity of CAH to CR decreased significantly. It knows that CR is an anionic azo dye. There are negative charges in the aqueous solution. In the pH range of 5-9, there are many positive charges on the surface of CAH. The electrostatic attraction between CR and CAH enhances the adsorption and the adsorption capacity is high. But when the pH value is too high, the solution will be alkaline, and there will be a large number of hydroxide anions. On the one hand, hydroxide anions will compete with SO_3^{2-} in CR to grab the active adsorption sites on the CAH surface. It hinders the adsorption of CR by CAH. On the other hand, there will be a considerable repulsive force between the same ions, and the repelling effect of hydroxide anions on the SO_3^{2-} in CR greatly weakens the adsorption between CAH and CR. Under the negative influence of these two aspects, the adsorption

capacity of CAH to CR has dropped significantly.

3.2.5 Swelling analysis

Observing Figure 8(e), it can be found that the swelling rate of CAH in distilled water shows a trend of first increasing and then decreasing with the increase of time. It has a maximum value at 20 minutes, the swelling rate is 16.2%, and the swelling rate increases with time. Decrease gradually, and finally the swelling rate remains at about 4.5% after 50 minutes. At first, due to the internal and external osmotic pressure of CAH, water molecules continue to enter the CAH. As water enters the CAH, the aluminum plasma on the internal structure of the CAH falls off, making the internal ionic strength of the CAH higher than the outside, and the resulting osmotic pressure makes more water It enters the inside of CAH, so before 20 minutes, the swelling rate of CAH in distilled water increases with time until it reaches the maximum value at 20 minutes. The swelling rate of CAH in CR solution also shows a trend of first increasing and then decreasing with the increase of time. It has a maximum value at 30 minutes, and the swelling rate is 20%. Then the swelling rate gradually decreases with time, and finally swells after 50 minutes. The rate remains unchanged at 6.6%. It is also because of the osmotic pressure inside and outside CAH that the swelling rate gradually increases until it reaches the maximum value at 30 min. Subsequently, as the internal and external aluminum ion strength of CAH gradually balances, the swelling rate of CAH in water and CR solution gradually decreases. The final swelling equilibrium is reached at 20min and 30min, respectively.

Before reaching the maximum swelling rate value, in the first 10 minutes, the swelling rate of CAH in distilled water is higher than its swelling rate in CR solution. This is because the CR molecules in the CR aqueous solution and various functional groups on the CAH surface will pass through each other. This kind of force causes it to be adsorbed on the surface of CAH, which prevents water molecules from entering the inside of CAH, so at first the swelling rate in CR aqueous solution is lower than that in distilled water. However, the maximum swelling rate and the final equilibrium swelling rate in the CR aqueous solution are higher than the swelling rate in distilled water. This is because in the CR solution, not only water will enter the CAH, but the CR molecules will also undergo electrostatic adsorption, hydrogen bonding, and aromatic The π - π conjugation between the rings causes the CR to be adsorbed inside the CAH, and with the continuous entry of water and CR, the aluminum ions on the internal structure of the CAH will fall off to form aluminum hydroxide colloid, which will interact with CR Flocculation occurred and settled.

3.2.6 Adsorption kinetics

The purpose of this study is to determine the kinetic model of the CR adsorption isotherm on CHA and to determine whether the adsorption of CR on the CAH adsorbent is good. It allows us to determine not only the time required to reach the adsorption equilibrium, but also the equilibrium constant of methylene blue adsorption. When the adsorbent dosage is 10mg, the CR concentration is 400mg/L, the adsorption temperature is 30°C, and the pH=7, the adsorbent CAH can reach a rapid adsorption equilibrium after 40 minutes. From the perspective of kinetics, the adsorption process is divided into two stages: fast reaction and slow reaction. In the first 30 minutes, more than 98% of CR was adsorbed on the CAH adsorbent. After 30 minutes, the speed slowed down slightly until 40 minutes, which is equivalent to the equilibrium time. The study of kinetic adsorption characteristics can help us obtain relevant adsorption rate data and help us better explain the adsorption mechanism. The kinetic adsorption equation was established under the conditions of 30°C and pH=6. The pseudo-first-order adsorption rate kinetic equation and the pseudo-second-order adsorption rate kinetic equation were used to fit and analyze the obtained data. The quasi-first-order (5) and quasi-second-order (6) are expressed as^[45]:

$$\ln(q_e - q_t) = \ln q_e - K_1 t \quad (3)$$

$$\frac{t}{q_t} = \frac{1}{K_2 q_e^2} + \frac{t}{q_e} \quad (4)$$

$$q_t = K_{id} t^{1/2} + C \quad (5)$$

Among them, q_t ($\text{mg}\cdot\text{g}^{-1}$) and q_e ($\text{mg}\cdot\text{g}^{-1}$) are the adsorption capacity of CR at time t (min) and equilibrium, respectively. K_1 (min^{-1}) and K_2 ($\text{g}\cdot\text{mg}^{-1}\cdot\text{min}^{-1}$) are the equilibrium rate constants of quasi-first-order and quasi-second-order, respectively. K_{id} ($\text{g}\cdot\text{mg}^{-1}\cdot\text{min}^{-1}$) is the internal diffusion rate constant. $t^{1/2}$ is the time point square root. C is a constant whose value is related to the thickness of the relevant boundary layer.

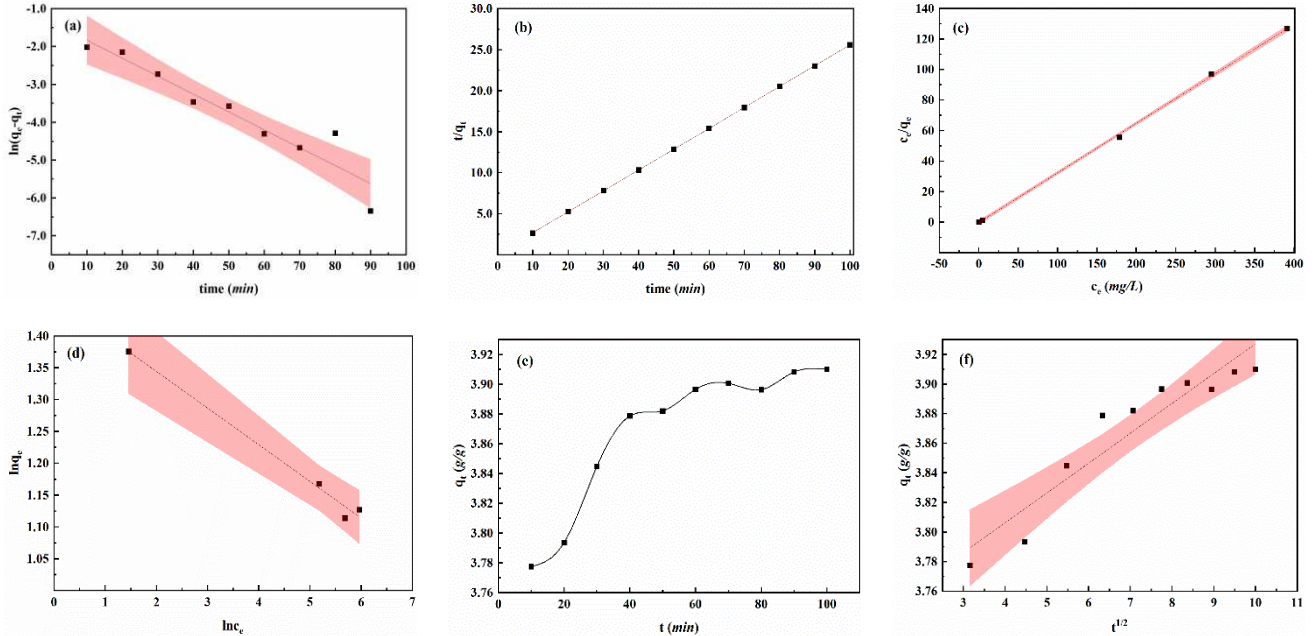


Fig.9 Kinetics of adsorption of CR by CAH Composite: first order kinetics (a); second order kinetics(b), Langmuir(c) and Freundlich(d) adsorption isotherm model; The adsorption-time curve (e) and intraparticle diffusion model(f) of CAH.

The kinetic parameters calculated by formulas (3, 4) are shown in Fig. 9 (a, b) and Table 2. It can be seen that the quasi-first-order model have a poor fit and low correlation coefficient ($R^2=0.9059$), while the quasi- second-order model has a good fit and high correlation coefficient ($R^2=0.9999$). The results show that the FCH adsorption of CR conforms to the pseudo- second-order model, but not the pseudo-first-order model.

Table. 2 Kinetic parameters of adsorption

$C_0(\text{mg/L})$	$q_e(\text{g}\cdot\text{g}^{-1})$	Pseudo-first-order		Pseudo-second-order	
		$K_1(\text{min}^{-1})$	R^2	$K_2(\text{g}\cdot\text{g}^{-1}\cdot\text{min}^{-1})$	R^2
400	3.9100	0.0474	0.9059	0.4385	0.9999

The adsorption capacity of CR by CAH at different adsorption times is shown in Figure 9(e). It can be found that with the increase of time, the adsorption capacity of CAH for CR also increases. The adsorption of CR by CAH is about 40 minutes, and the equilibrium adsorption capacity is about 3.91 g/g. In addition, Figure 9(f) adopts a particle diffusion model for the adsorption process of CR by CAH. Further research found that the graph does not pass through the origin and is not completely linear, which indicates that intra-particle diffusion is not the only rate control step. The relevant parameters are shown in Table 3. The internal diffusion rate constant of CAH to CR is $0.0202 \text{ g}\cdot\text{g}^{-1}\cdot\text{min}^{-1}$.

Table. 3 Correlation coefficients for the intraparticle diffusion model of CAH

$C_0(\text{mg/L})$	$K_{id}(\text{g}\cdot\text{g}^{-1}\cdot\text{min}^{-1})$	$C(\text{g/g})$	R^2
400	0.0202	3.7255	0.8896

3.2.7 Adsorption isotherms

Exploring the relationship between the adsorption capacity of the prepared FCH and the initial concentration, measuring the adsorption capacity of FCH on MB under different initial concentrations, and discussing its thermodynamic adsorption characteristics, so that relevant isotherm adsorption model data can be obtained. The adsorption model equation and Freundlich isotherm adsorption equation are used to fit and analyze the data obtained. Langmuir (7) and Freundlich (8) isotherm adsorption model equations are as follows^[46]:

$$\frac{c_e}{q_e} = \frac{1}{K_L q_m} + \frac{c_e}{q_m} \quad (5)$$

$$\ln q_e = \ln K_F + \frac{1}{n} \ln c_e \quad (6)$$

where q_e (g/g) and q_m (g/g) are equilibrium adsorption capacity and maximum adsorption capacity, respectively. c_e (mg/L) is the equilibrium concentration of CR solution. K_F (L/mg) and n are the Freundlich constants.

Table. 4 Isotherm parameters of adsorption

CAH	Langmuir			Freundlich		
	K_L (L/mg)	q_m (g/g)	R^2	K_F (L·mg ⁻¹)	n	R^2
	-1.1223	3.0788	0.9996	4.3033	-17.3671	0.9835

Figure 9(b, c) is Langmuir and Freundlich isotherms, and the relevant thermodynamic parameters are listed in Table 4. It can be readily seen that the Langmuir model is more adaptable than the Freundlich model. The $R^2=0.9996$ of the Langmuir model is much larger than the $R^2=0.9835$ of the Freundlich model, indicating that the Langmuir model is very well supplied. It shows that the CAH adsorption of CR is a single layer adsorption, and the CAH surface-active sites are evenly distributed.

3.2 Study on adsorption mechanism

The related adsorption mechanism of CR by CAH is illustrated in Figure 10. According to the adsorption model, CAH mainly adsorbed CR on the monolayer. On the one hand, the cation Al^{3+} and CR anions on the CAH surface adsorbed CR on the CAH surface by electrostatic gravitation. On the other hand, it is found that the surface of CAH contains a large number of -OH functional groups, while CR is a typical azo molecule and contains highly electronegative nitrogen atoms. In addition, FT-IR and XPS results show that there are a lot of C=O in CAH, and a certain degree of unsaturation in CR.

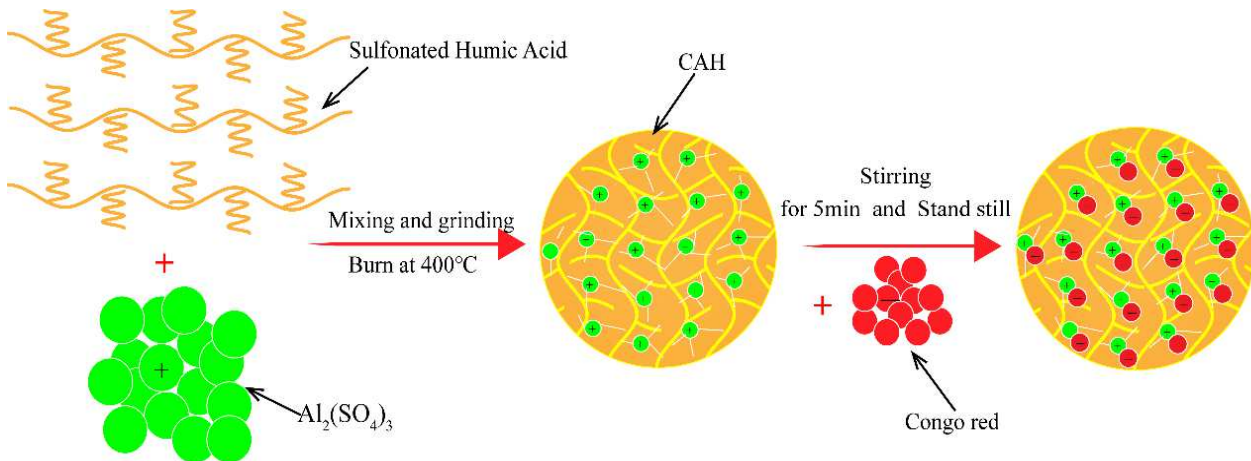


Fig.10 CAH adsorption CR mechanism diagram

The previous analysis of the swelling behavior of CAH shows that water molecules enter the interior of CAH and

CR is adsorbed on the surface of CAH. On the one hand, Al^{3+} and CR molecules in the cross-linked structure of CAH network combine with electrostatic gravitation and complexation to make CR adsorbed into the interior. On the other hand, due to the increase of the volume and expansion of CAH particles due to the entry of water, the pore channels and network cross-linking structure in CAH are more favorable for CR to enter into CAH and react with internal groups and ions. According to the observation of the adsorption process, it is found that there are flocs in the solution, which is that Al^{3+} in the cross-linked structure of CAH network breaks away from CAH and permeates into CR solution to form $\text{Al}(\text{OH})_3$ colloid, $\text{Al}(\text{OH})_3$ colloid through electro neutralization and CR anion adsorption bridging action to remove CR from the solution. In addition, according to the isothermal adsorption model, it is shown that the adsorption process of CAH to CR is monolayer adsorption. When the first layer of molecules reaches saturation on the surface and enters the interior of CAH, CAH will form a new surface, and new CR molecules in the solution will be adsorbed on the surface, and finally all CR will be removed.

4. Conclusions

Humic acid and aluminum sulfate are used as raw materials to prepare humic acid-based aluminum-carbon composite material (CAH) by high-temperature oxidation-reduction method, which is used as an efficient adsorbent to remove the anionic dye wastewater Congo red (CR) in aqueous solution. TEM and SEM show that CAH has a large number of uneven porous structures. FT-IR, XRD, Raman and XPS characterize the elemental composition and bonding mode of CAH. A large number of Al-O bonds are generated in CAH, which increases a large number of active sites for adsorption. TG-DSC shows that CAH has better thermal stability than HA. Moreover, after 400°C , the pyrolysis rate increased sharply, including various free radical fragmentation and recombination. BET shows that CAH has a large specific surface area, but the pore size is relatively large, which is a mesoporous material. The results of adsorption experiments show that under alkaline conditions, the pH value has a great influence on the adsorption capacity of CAH. As the pH increases, the adsorption capacity decreases; under acidic and neutral conditions, the pH value has almost no effect on the adsorption capacity. The adsorption capacity of CAH is approximately 3.98g/g . When the temperature is between $10\text{-}30^\circ\text{C}$, the adsorption capacity increases as the temperature rises. When the temperature is greater than 30°C , the adsorption capacity begins to decrease. The adsorption of CR by CAH follows a quasi-two-stage kinetic model, the equilibrium adsorption isotherm is more in line with the Langmuir model, and the adsorption of CR by CAH is more inclined to single-layer adsorption. The adsorption process is good, the CR molecule and CAH have a strong bonding ability, and have a great adsorption capacity. It has broad application prospects in the treatment of printing and dyeing wastewater pollutants.

Acknowledgements

This study was funded by the key R&D project of Hebei Province, China, "Caofeidian Port Dredged Land Resource Utilization Key Technology Integration and Demonstration". [project number 20373805D, 202006-202112].

Compliance with ethical standards

Conflict of interest The authors declare that they have no conflict of interest.

Reference

- [1] P. Oulego, A. Laca, S. Calvo, M. Díaz, Eggshell-supported catalysts for the advanced oxidation treatment of humic acid polluted wastewaters, *Water (Switzerland)*. 12 (2020). <https://doi.org/10.3390/w12010100>.
- [2] M.A. Islam, I. Ali, S.M.A. Karim, M.S. Hossain Firoz, A.N. Chowdhury, D.W. Morton, M.J. Angove, Removal of dye from polluted water using novel nano manganese oxide-based materials, *J. Water Process Eng.* 32 (2019) 100911. <https://doi.org/10.1016/j.jwpe.2019.100911>.
- [3] M.A. Mamelkina, M. Herraiz-Carboné, S. Cotillas, E. Lacasa, C. Sáez, R. Tuunila, M. Sillanpää, A. Häkkinen, M.A. Rodrigo, Treatment of mining wastewater polluted with cyanide by coagulation processes: A mechanistic study, *Sep. Purif. Technol.* 237 (2020) 116345. <https://doi.org/10.1016/j.seppur.2019.116345>.
- [4] A. Kazemi, N. Bahramifar, A. Heydari, S.I. Olsen, Synthesis and sustainable assessment of thiol-functionalization of magnetic graphene oxide and superparamagnetic Fe₃O₄@SiO₂ for Hg(II) removal from aqueous solution and petrochemical wastewater, *J. Taiwan Inst. Chem. Eng.* 95 (2019) 78–93. <https://doi.org/10.1016/j.jtice.2018.10.002>.
- [5] Y. Shao, H. Pei, W. Hu, C.P. Chanway, P. Meng, Y. Ji, Z. Li, Bioaugmentation in lab scale constructed wetland microcosms for treating polluted river water and domestic wastewater in northern China, *Int. Biodeterior. Biodegrad.* 95 (2014) 151–159. <https://doi.org/10.1016/j.ibiod.2014.05.027>.
- [6] Y. Yan, H. Yang, Z. Yi, R. Li, T. Xian, Design of ternary CaTiO₃/g-C₃N₄/AgBr Z-scheme heterostructured photocatalysts and their application for dye photodegradation, *Solid State Sci.* 100 (2020) 106102. <https://doi.org/10.1016/j.solidstatesciences.2019.106102>.
- [7] G. Niero, A.X.R. Corrêa, G. Trierweiler, A.J.F. Matos, R. Corrêa, H.A.G. Bazani, C.M. Radetski, Using modified fish scale waste from *Sardinella brasiliensis* as a low-cost adsorbent to remove dyes from textile effluents, *J. Environ. Sci. Heal. - Part A Toxic/Hazardous Subst. Environ. Eng.* 54 (2019) 1083–1090. <https://doi.org/10.1080/10934529.2019.1631091>.
- [8] B. Bharathiraja, I.A. Ebenezer Selvakumari, J. Iyyappan, S. Varjani, Itaconic acid: an effective sorbent for removal of pollutants from dye industry effluents, *Curr. Opin. Environ. Sci. Heal.* 12 (2019) 6–17. <https://doi.org/10.1016/j.coesh.2019.07.004>.
- [9] S. Ravulapalli, K. Ravindhranath, Effective removal of methylene blue, a hazardous dye from industrial effluents using active carbon of *F.infectoria* plant, *Int. J. Environ. Sci. Technol.* 16 (2019) 7837–7848. <https://doi.org/10.1007/s13762-018-2147-3>.
- [10] C.W. Chiu, M.T. Wu, J.C.M. Lee, T.Y. Cheng, Isothermal adsorption properties for the adsorption and removal of reactive Blue 221 dye from aqueous solutions by cross-linked β -chitosan glycan as acid-resistant adsorbent, *Polymers (Basel)*. 10 (2018). <https://doi.org/10.3390/polym10121328>.
- [11] L. Aljerf, High-efficiency extraction of bromocresol purple dye and heavy metals as chromium from industrial effluent by adsorption onto a modified surface of zeolite: Kinetics and equilibrium study, *J. Environ. Manage.* 225 (2018) 120–132. <https://doi.org/10.1016/j.jenvman.2018.07.048>.
- [12] A.A. Inyinbor, F.A. Adekola, O.A. Dada, A.P. Oluyori, G.A. Olatunji, O.F. Fanawopo, T.A. Orefofe, T.O. Abodunrin, Novel acid treated biomass: Applications in Cu[Formula presented] scavenging, Rhodamine B/Cu[Formula presented] binary solution and real textile effluent treatment, *Environ. Technol. Innov.* 13 (2019) 37–47. <https://doi.org/10.1016/j.eti.2018.10.006>.
- [13] A.E. Al Prol, Study of Environmental Concerns of Dyes and Recent Textile Effluents Treatment Technology: A Review, *Asian J. Fish. Aquat. Res.* 3 (2019) 1–18. <https://doi.org/10.9734/ajfar/2019/v3i230032>.
- [14] A. Dimitrijević, A. Jocić, N. Zec, A. Tot, S. Papović, S. Gadžurić, M. Vraneš, T. Trtić-Petrović, Improved single-step extraction performance of aqueous biphasic systems using novel symmetric ionic liquids for the decolorisation of toxic dye effluents, *J. Ind. Eng. Chem.* 76 (2019) 500–507. <https://doi.org/10.1016/j.jiec.2019.04.017>.
- [15] R. Wang, C. Yang, K. Fang, Y. Cai, L. Hao, Removing the residual cellulase by graphene oxide to recycle the bio-polishing effluent for dyeing cotton fabrics, *J. Environ. Manage.* 207 (2018) 423–431.

<https://doi.org/10.1016/j.jenvman.2017.11.056>.

- [16] W. Wang, J. Ni, L. Chen, Z. Ai, Y. Zhao, S. Song, Synthesis of carboxymethyl cellulose-chitosan-montmorillonite nanosheets composite hydrogel for dye effluent remediation, Elsevier B.V, 2020. <https://doi.org/10.1016/j.ijbiomac.2020.09.154>.
- [17] K. Maheshwari, Y.S. Solanki, M.S.H. Ridoy, M. Agarwal, R. Dohare, R. Gupta, Ultrasonic treatment of textile dye effluent utilizing microwave-assisted activated carbon, *Environ. Prog. Sustain. Energy*. 39 (2020). <https://doi.org/10.1002/ep.13410>.
- [18] T. Farahmand, S. Hashemian, A. Sheibani, ZIF-based zinc titanate composite as sufficient sorbent for removal of Congo red from aqueous solutions, *J. Asian Ceram. Soc.* 8 (2020) 721–732. <https://doi.org/10.1080/21870764.2020.1780718>.
- [19] L. Wen, X. Chen, C. Chen, R. Yang, M. Gong, Y. Zhang, Q. Fu, Ice-templated porous polymer/UiO-66 monolith for Congo Red adsorptive removal, *Arab. J. Chem.* 13 (2020) 5669–5678. <https://doi.org/10.1016/j.arabjc.2020.04.007>.
- [20] V.K. Gupta, S. Agarwal, R. Ahmad, A. Mirza, J. Mittal, Sequestration of toxic congo red dye from aqueous solution using ecofriendly guar gum/ activated carbon nanocomposite., *Int. J. Biol. Macromol.* 158 (2020) 1310–1318. <https://doi.org/10.1016/j.ijbiomac.2020.05.025>.
- [21] X. Guo, L. Kong, Y. Ruan, Z. Diao, K. Shih, M. Su, L. Hou, D. Chen, Green and facile synthesis of cobalt-based metal-organic frameworks for the efficient removal of Congo red from aqueous solution, *J. Colloid Interface Sci.* 578 (2020) 500–509. <https://doi.org/10.1016/j.jcis.2020.05.126>.
- [22] J. Wang, P. Sun, H. Xue, J. Chen, H. Zhang, W. Zhu, Red mud derived facile hydrothermal synthesis of hierarchical porous α -Fe₂O₃ microspheres as efficient adsorbents for removal of Congo red, *J. Phys. Chem. Solids.* 140 (2020) 109379. <https://doi.org/10.1016/j.jpcs.2020.109379>.
- [23] Faheem, J. Du, J. Bao, M.A. Hassan, S. Irshad, M.A. Talib, Multi-functional Biochar Novel Surface Chemistry for Efficient Capture.pdf, *Arab. J. Sci. Eng.* (2019).
- [24] S. ARUL, T. SENTHILNATHAN, Kinetics and Photodegradation Study of Congo Red using Mg with Ti/Al Co-Doped ZnO Nanocomposite under UV Light, *Asian J. Chem.* 32 (2020) 369–373.
- [25] Z. Gün Gök, K. Günay, M. Arslan, M. Yiğitoğlu, Removing of Congo red from aqueous solution by 2-hydroxyethyl methacrylate-g-poly(ethylene terephthalate) fibers, *Polym. Bull.* 76 (2019) 6179–6191. <https://doi.org/10.1007/s00289-019-02721-2>.
- [26] Y. Yue, Z. Cao, F. Yang, J. Wang, I. Abrahams, Preparation of an Anti-Aggregation Silica/Zinc/Graphene Oxide Nanocomposite with Enhanced Adsorption Capacity, *Chem. - A Eur. J.* 25 (2019) 16340–16349. <https://doi.org/10.1002/chem.201903875>.
- [27] X. Wei, Y. Wang, Y. Feng, X. Xie, X. Li, S. Yang, Different adsorption-degradation behavior of methylene blue and Congo red in nanoceria/H₂O₂ system under alkaline conditions, *Sci. Rep.* 9 (2019) 2–11. <https://doi.org/10.1038/s41598-018-36794-2>.
- [28] F. Yu, X. Bai, M. Liang, J. Ma, Recent progress on metal-organic framework-derived porous carbon and its composite for pollutant adsorption from liquid phase, *Chem. Eng. J.* 405 (2021) 126960. <https://doi.org/10.1016/j.cej.2020.126960>.
- [29] Y.D. Dong, H. Zhang, G.J. Zhong, G. Yao, B. Lai, Cellulose/carbon Composites and their Applications in Water Treatment – a Review, *Chem. Eng. J.* 405 (2021) 126980. <https://doi.org/10.1016/j.cej.2020.126980>.
- [30] Y. Wu, Y. Huang, H. Huang, Y. Muhammad, Z. Huang, J. Winarta, Y. Zhang, S. Nie, Z. Zhao, B. Mu, Porous Fe@C Composites Derived from Silkworm Excrement for Effective Separation of Anisole Compounds, *ACS Omega.* 4 (2019) 21204–21213. <https://doi.org/10.1021/acsomega.9b02681>.
- [31] C.H. Zhou, L. Cun Jun, W.P. Gates, T.T. Zhu, Y. Wei Hua, Co-intercalation of organic cations/amide molecules into montmorillonite with tunable hydrophobicity and swellability, *Appl. Clay Sci.* 179 (2019). <https://doi.org/10.1016/j.clay.2019.105157>.
- [32] X. Zhang, L. Cheng, X. Wu, Y. Tang, Y. Wu, Activated carbon coated palygorskite as adsorbent by activation and its adsorption for methylene blue, *J. Environ. Sci. (China)*. 33 (2015) 97–105. <https://doi.org/10.1016/j.jes.2015.01.014>.

- [33] A.A. Narvekar, J.B. Fernandes, S.G. Tilve, Adsorption behavior of methylene blue on glycerol based carbon materials, *J. Environ. Chem. Eng.* 6 (2018) 1714–1725. <https://doi.org/10.1016/j.jece.2018.02.016>.
- [34] L. Dali Youcef, L.S. Belaroui, A. López-Galindo, Adsorption of a cationic methylene blue dye on an Algerian palygorskite, *Appl. Clay Sci.* 179 (2019) 105145. <https://doi.org/10.1016/j.clay.2019.105145>.
- [35] C. Liu, W. Cai, L. Liu, Hydrothermal carbonization synthesis of Al-pillared montmorillonite@carbon composites as high performing toluene adsorbents, *Appl. Clay Sci.* 162 (2018) 113–120. <https://doi.org/10.1016/j.clay.2018.06.005>.
- [36] X. Yang, F. Li, M. Xia, F. Luo, Y. Jiang, Investigation on the micro-structure and adsorption capacity of cellulosic biomass carbon based montmorillonite composite, *Microporous Mesoporous Mater.* 256 (2018) 18–24. <https://doi.org/10.1016/j.micromeso.2017.07.052>.
- [37] Y. Li, A.R. Zimmerman, F. He, J. Chen, L. Han, H. Chen, X. Hu, B. Gao, Solvent-free synthesis of magnetic biochar and activated carbon through ball-mill extrusion with Fe₃O₄ nanoparticles for enhancing adsorption of methylene blue, *Sci. Total Environ.* 722 (2020) 137972. <https://doi.org/10.1016/j.scitotenv.2020.137972>.
- [38] F. Labbé, E. Disa, Y. Ahmad, K. Guérin, T. Asset, F. Maillard, M. Chatenet, R. Metkemeijer, S. Berthon-Fabry, Tin dioxide coated carbon materials as an alternative catalyst support for PEMFCs: Impacts of the intrinsic carbon properties and the synthesis parameters on the coating characteristics, *Microporous Mesoporous Mater.* 271 (2018) 1–15. <https://doi.org/10.1016/j.micromeso.2018.05.019>.
- [39] M. Anand, S.A. Farooqui, J. Singh, H. Singh, A.K. Sinha, Mechanistic in-operando FT-IR studies for hydroprocessing of triglycerides, *Catal. Today.* 309 (2018) 11–17. <https://doi.org/10.1016/j.cattod.2017.12.021>.
- [40] Y.T. Ng, W. Kong, I. Kong, Magnetite-functionalized graphene nanohybrids: Preparation and characterization of electrical and magnetic property, *Mater. Today Proc.* 5 (2018) 3202–3210. <https://doi.org/10.1016/j.matpr.2018.01.129>.
- [41] Z. Zhang, D. Niu, Y. Li, J. Shi, Magnetic, core-shell structured and surface molecularly imprinted polymers for the rapid and selective recognition of salicylic acid from aqueous solutions, *Appl. Surf. Sci.* 435 (2018) 178–186. <https://doi.org/10.1016/j.apsusc.2017.11.033>.
- [42] A. Wang, X. Sun, B. Li, H. Shang, Y. Jiang, Z. Zhao, Preparation of Carbon–Iron Composites Materials and Studies of Its Adsorption Properties for the Methylene Blue, *J. Inorg. Organomet. Polym. Mater.* (2020). <https://doi.org/10.1007/s10904-020-01754-9>.
- [43] Y. Yan, Y. Wei, Q. Li, M. Shi, C. Zhao, L. Chen, C. Fan, R. Yang, Y. Xu, Activated porous carbon materials with ultrahigh specific surface area derived from banana peels for high-performance lithium–sulfur batteries, *J. Mater. Sci. Mater. Electron.* 29 (2018) 11325–11335. <https://doi.org/10.1007/s10854-018-9220-z>.
- [44] B. Huang, J. He, S. Bian, C. Zhou, Z. Li, F. Xi, J. Liu, X. Dong, S-doped graphene quantum dots as nanophotocatalyst for visible light degradation, *Chinese Chem. Lett.* 29 (2018) 1698–1701. <https://doi.org/10.1016/j.ccllet.2018.01.004>.
- [45] J. Yang, Y. Dou, H. Yang, D. Wang, A novel porous carbon derived from CO₂ for high-efficient tetracycline adsorption: Behavior and mechanism, *Appl. Surf. Sci.* 538 (2021) 148110. <https://doi.org/10.1016/j.apsusc.2020.148110>.
- [46] G. Wang, T. Sun, Z. Sun, X. Hu, Preparation of copper based metal organic framework materials and its effective adsorptive removal of ceftazidime from aqueous solutions, *Appl. Surf. Sci.* 532 (2020) 147411. <https://doi.org/10.1016/j.apsusc.2020.147411>.

Figures

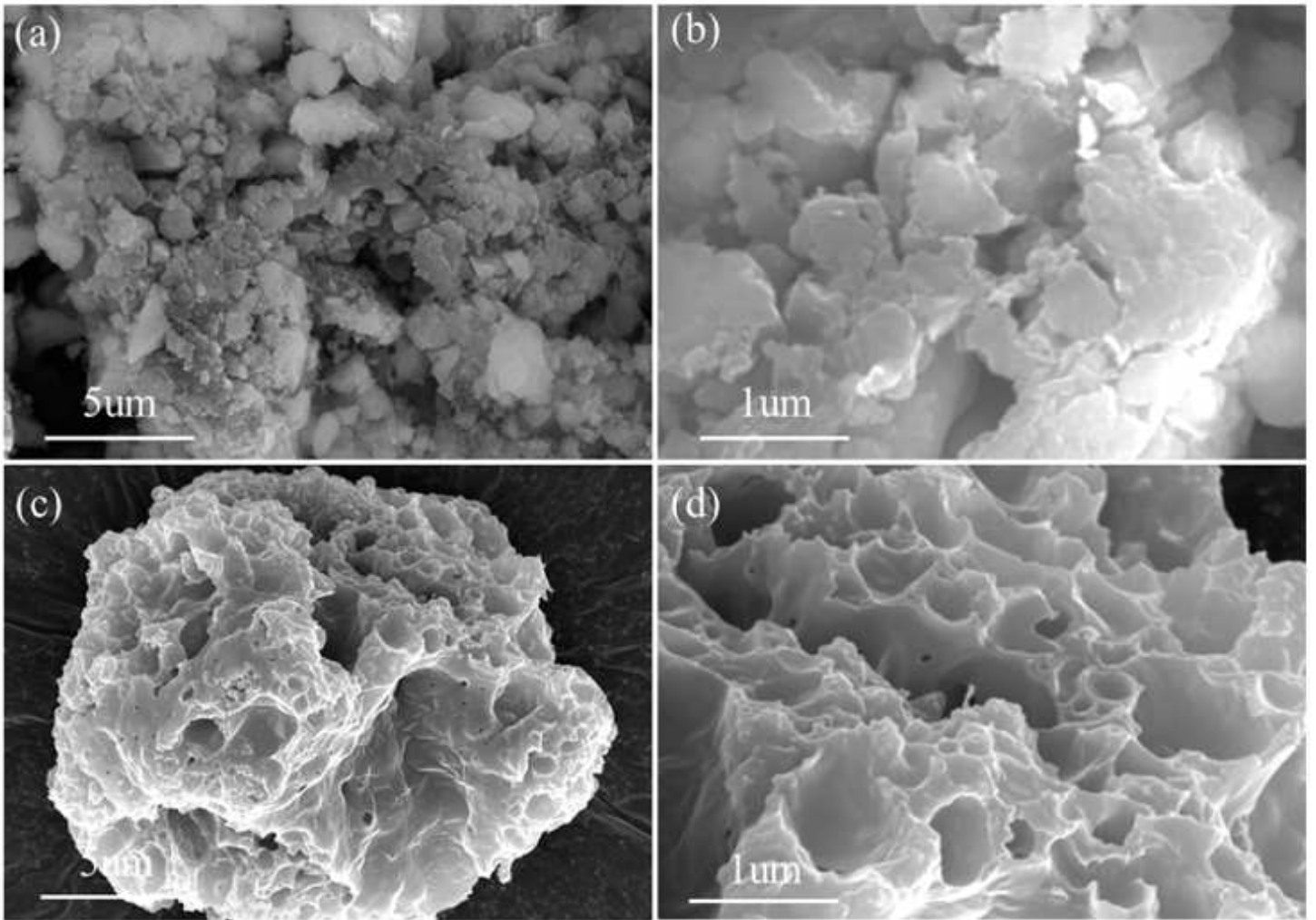


Figure 1

SEM of the HA (a, b) and CAH (c, d)

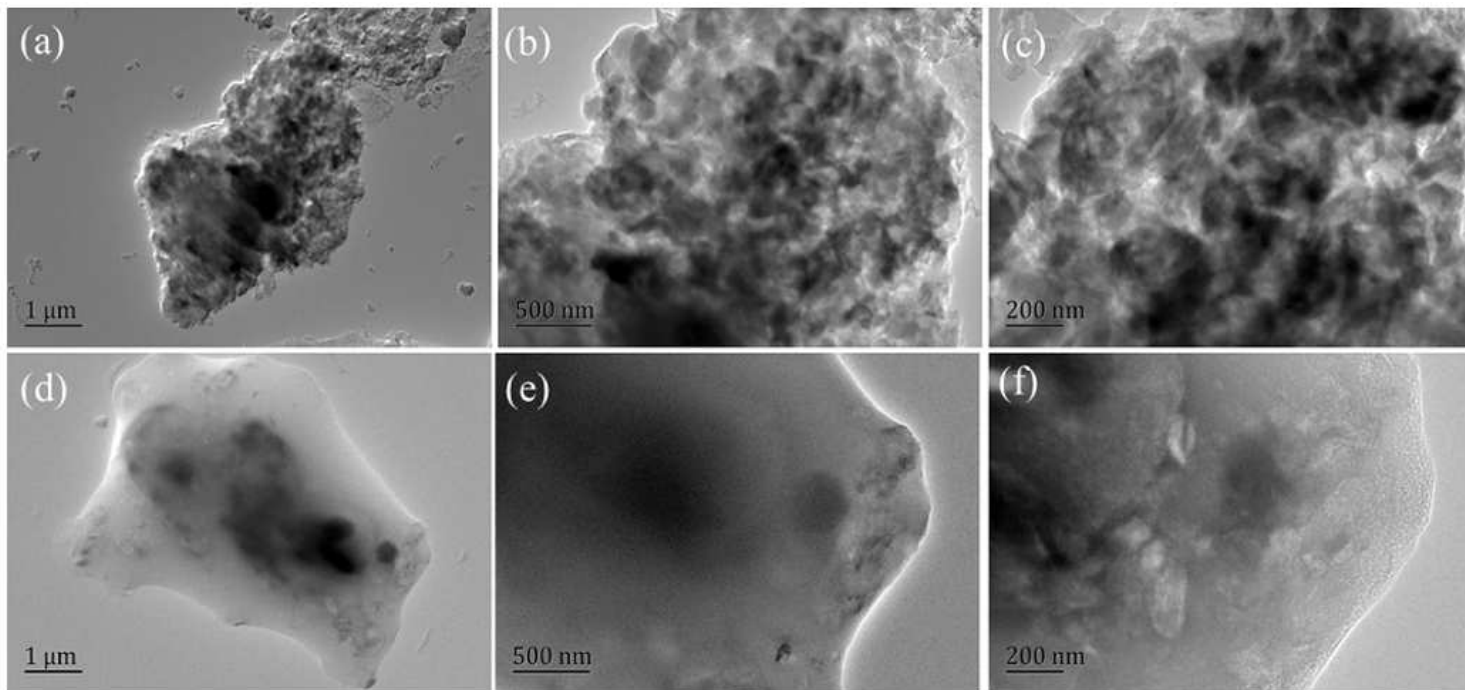


Figure 2

TEM of the HA (a, b, c) and CAH (d, e, f)

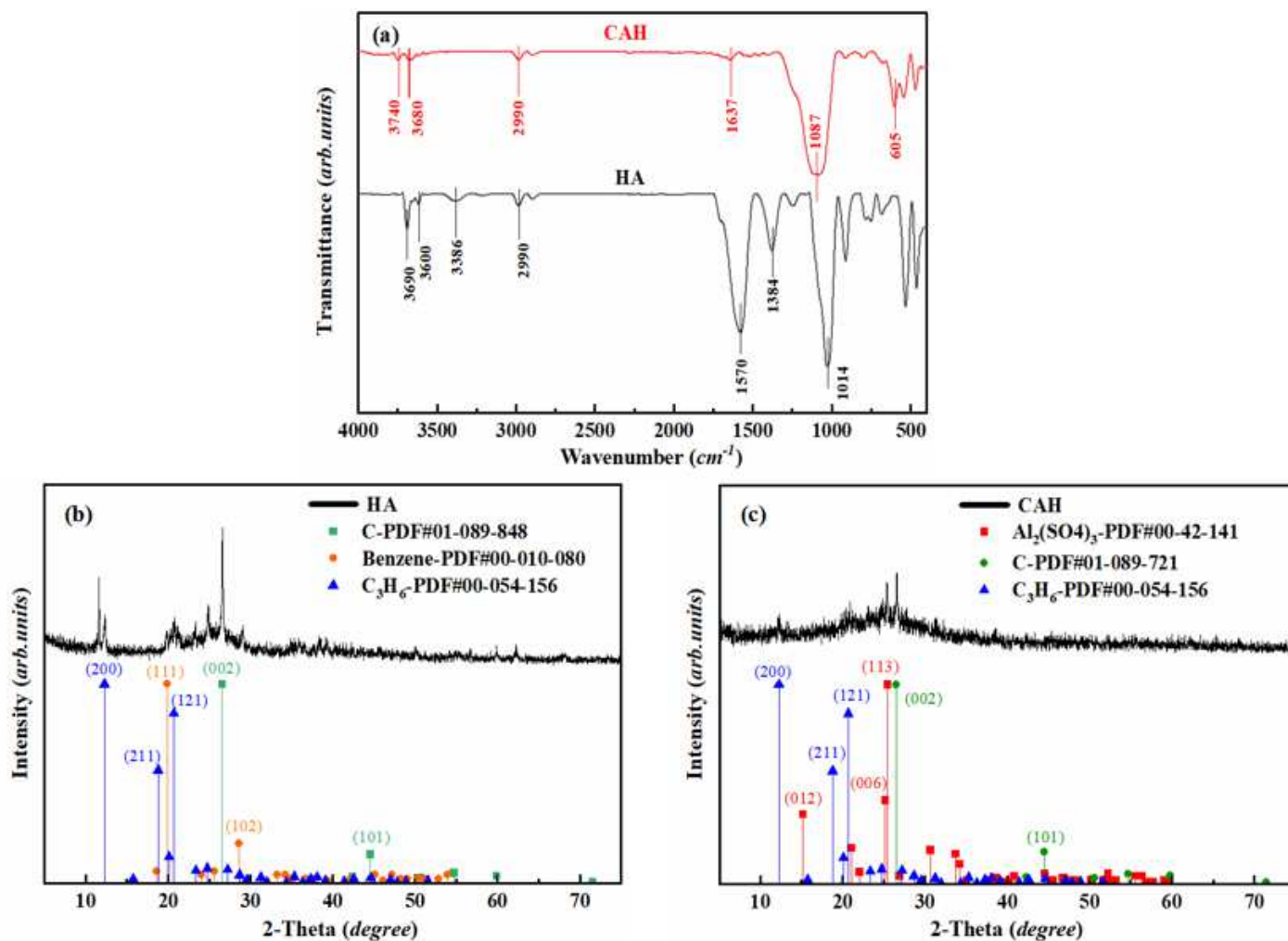


Figure 3

FT-IR of the HA and CAH (a); XRD patterns of HA and HA base peak (b), patterns of CAH and CAH base peak (c)

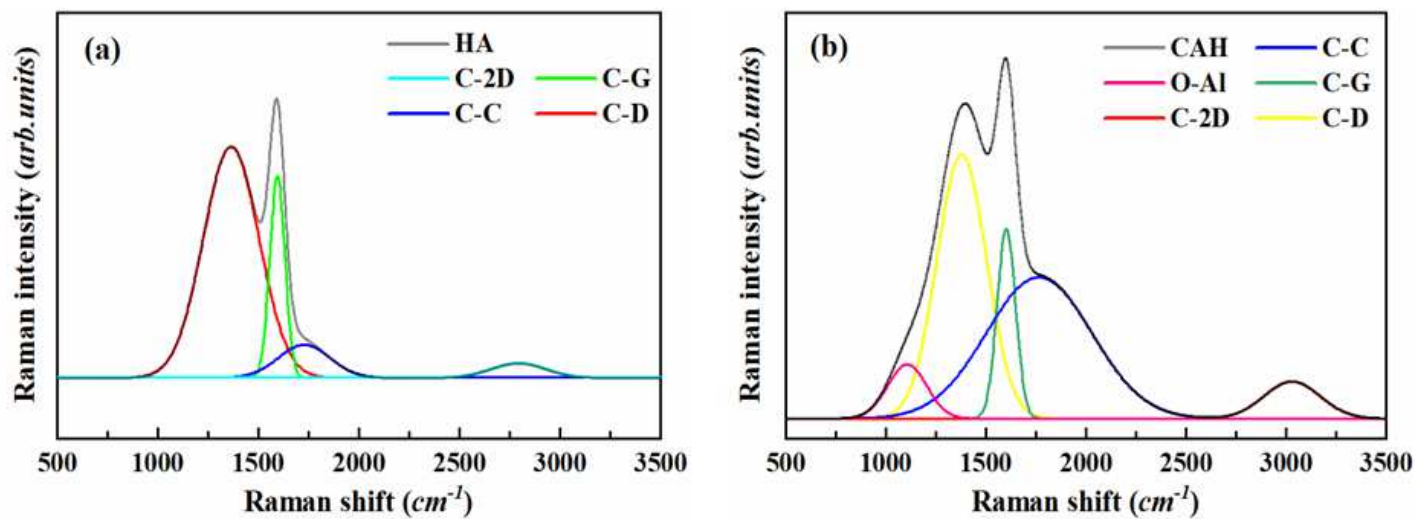


Figure 4

Raman spectrum of the HA (a) and CAH (b)

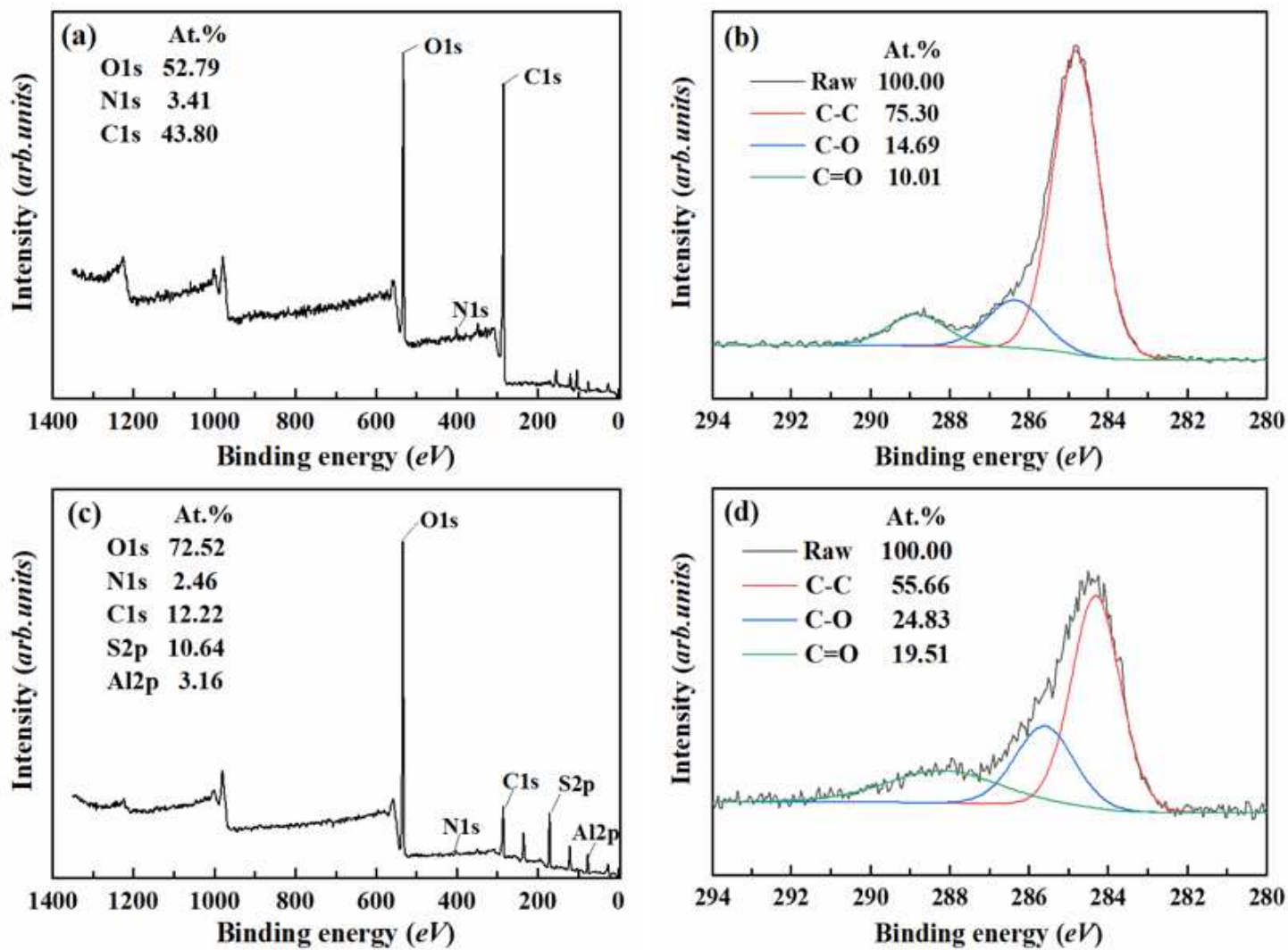


Figure 5

XPS total peaks of HA and CAH (a, c); C1s peaks of HA and CAH (b, d)

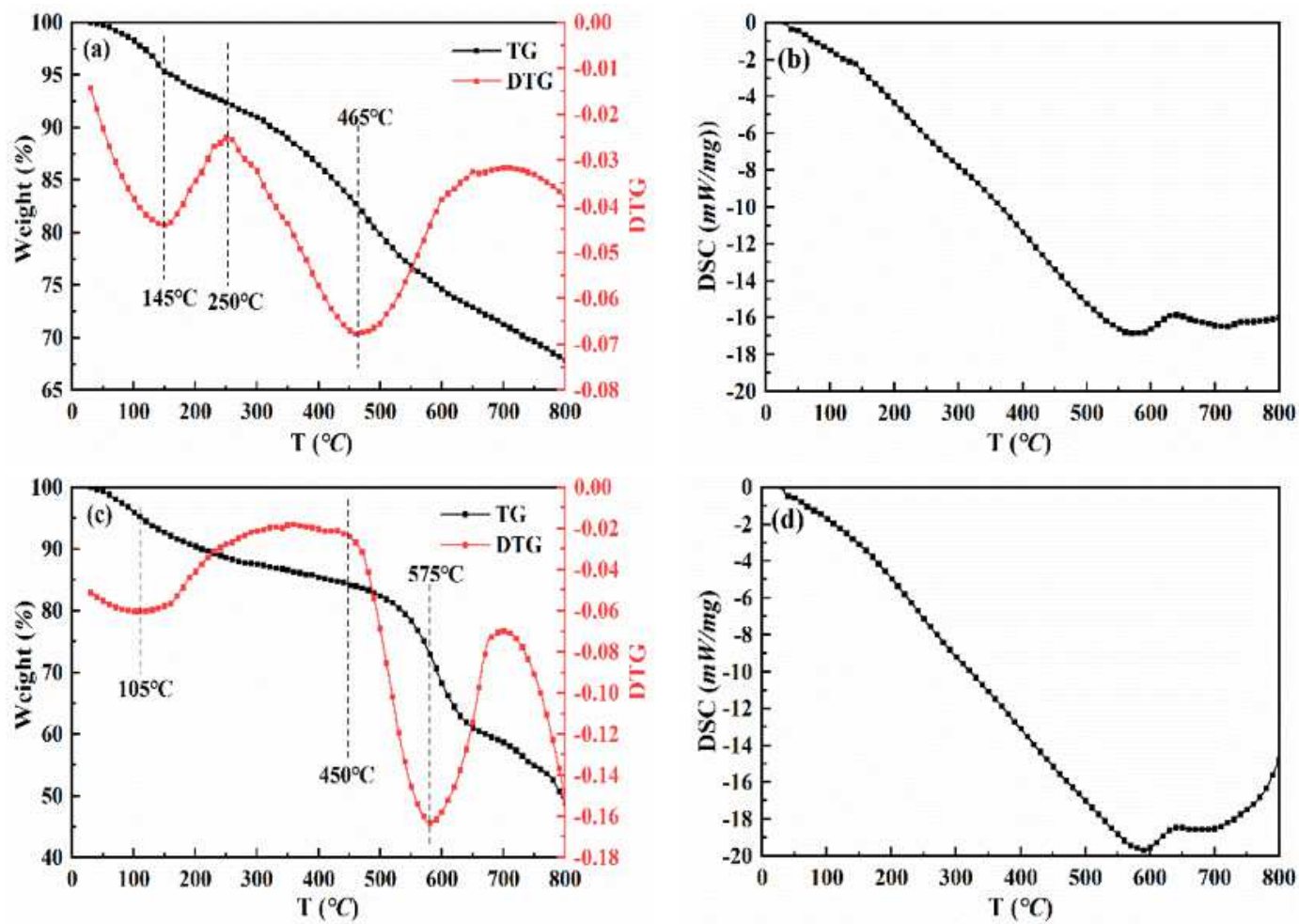


Figure 6

TG-DSC of the HA (a, b) and CAH (c, d)

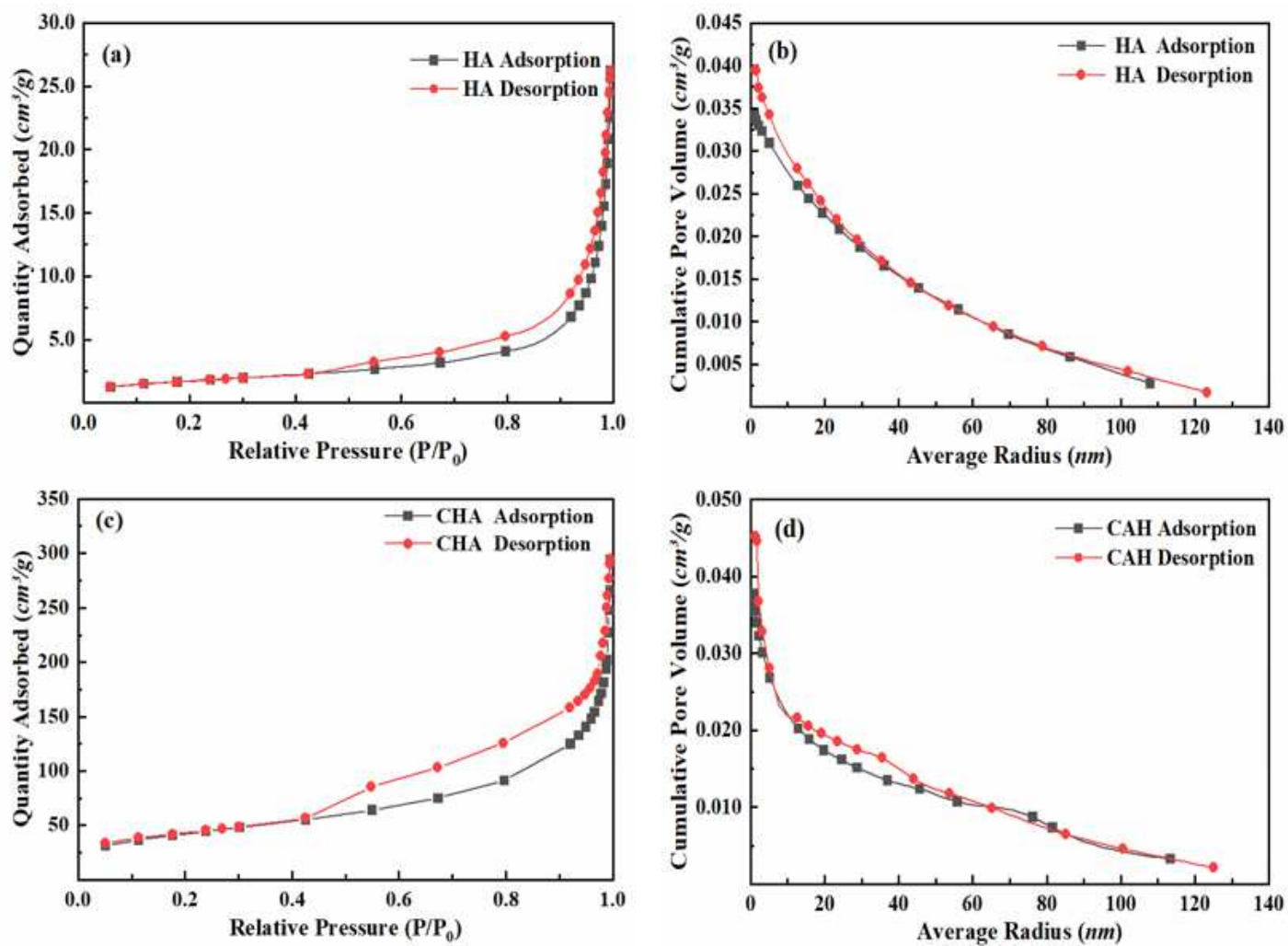


Figure 7

BET of the HA (a, b) and CAH (c, d)

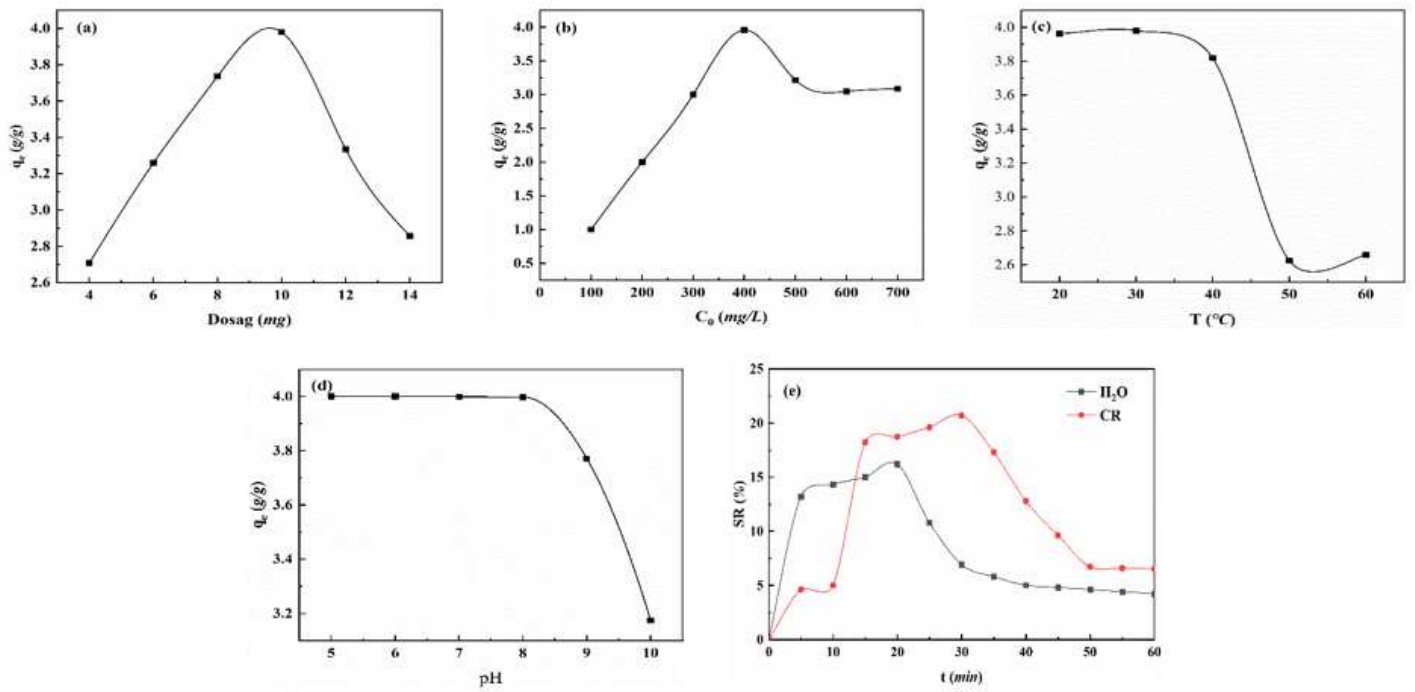


Figure 8

The effect of the initial concentration of CR on the adsorption capacity (a) and removal rate (b); the effect of temperature (c) and pH (d) on the adsorption capacity impact; the effect of time on SR of CAH (e).

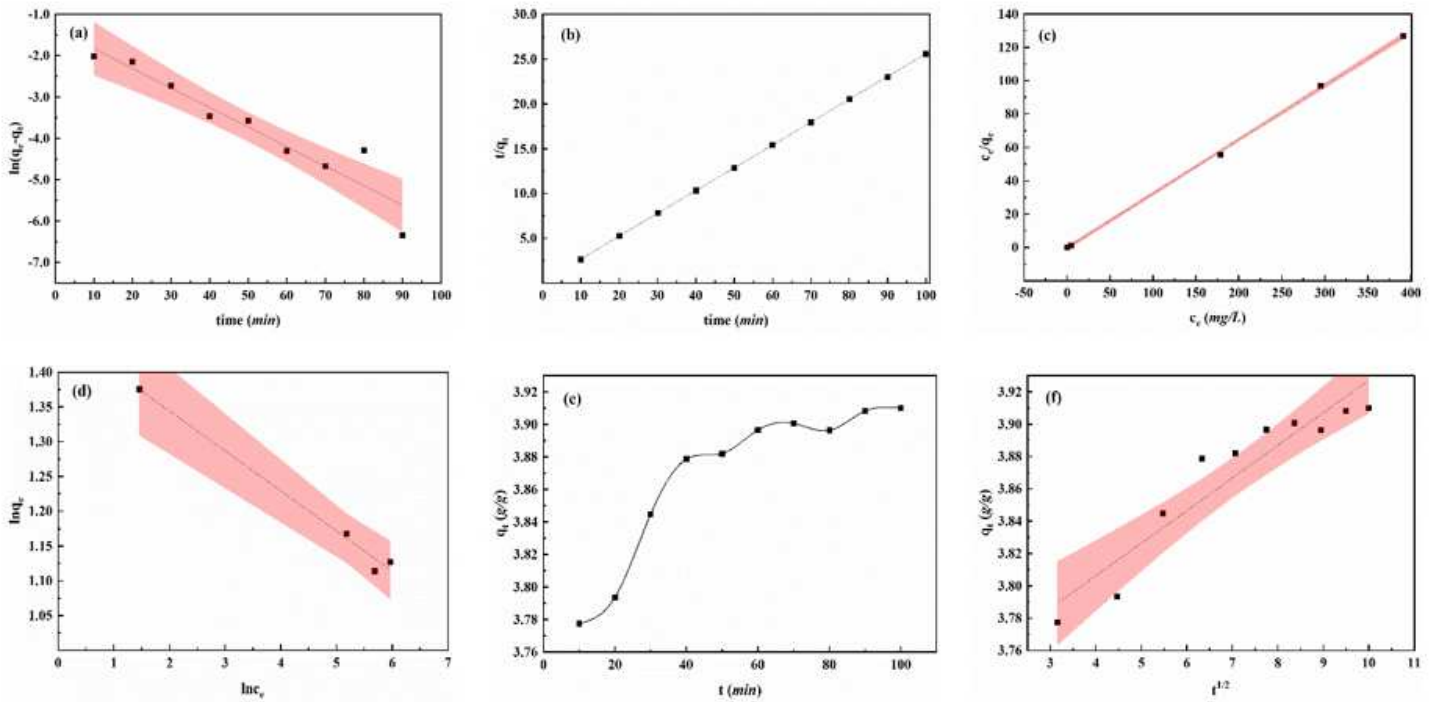


Figure 9

Kinetics of adsorption of CR by CAH Composite: first order kinetics (a); second order kinetics(b), Langmuir(c) and Freundlich(d) adsorption isotherm model; The adsorption-time curve (e) and

intraparticle diffusion model(f) of CAH.

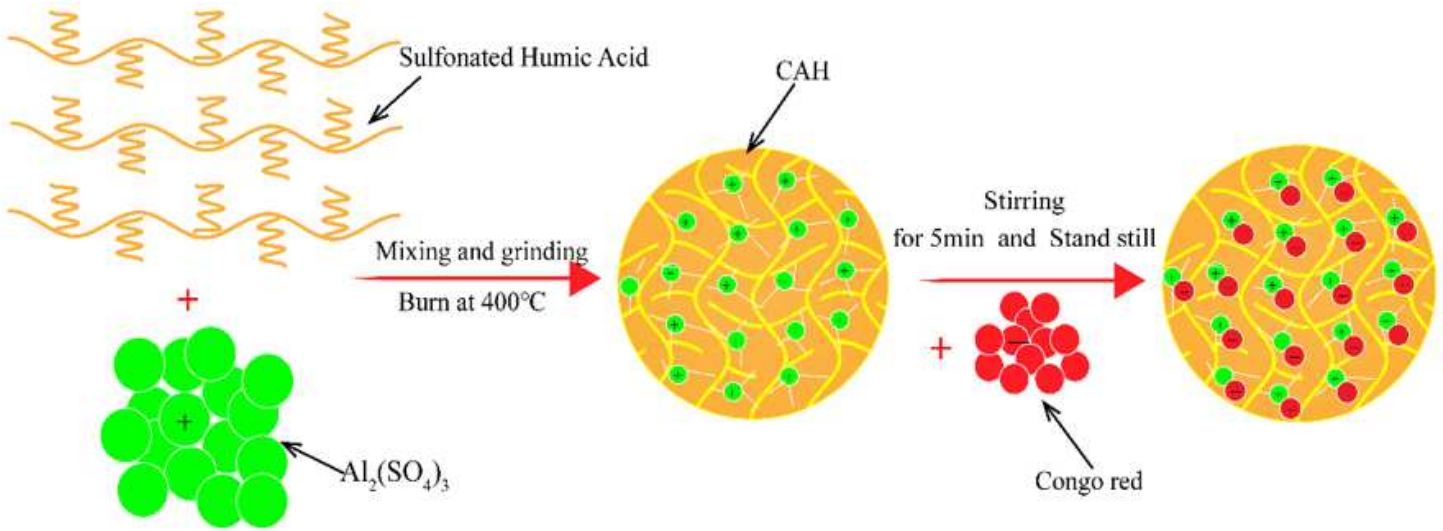


Figure 10

CAH adsorption CR mechanism diagram